Wave-driven hydrodynamics around a saltmarsh cliff under storm conditions the role of cliff height and vegetation

Muller, J. R.M.; Borsje, B. W.; van der Werf, J. J.; Dermentzoglou, D.; Hofland, B.; Antonini, A.; Hulscher, S. J.M.H.

DOI
10.1016/j.coastaleng.2025.104875

Publication date
2025

Document Version
Final published version

Published in
Coastal Engineering

Citation (APA)
Muller, J. R. M., Borsje, B. W., van der Werf, J. J., Dermentzoglou, D., Hofland, B., Antonini, A., & Hulscher, S. J. M. H. (2025). Wave-driven hydrodynamics around a saltmarsh cliff under storm conditions: the role of cliff height and vegetation. *Coastal Engineering*, *204*, Article 104875. https://doi.org/10.1016/j.coastaleng.2025.104875

Coastal Engineering 204 (2026) 104875

Contents lists available at ScienceDirect

Coastal Engineering

journal homepage: www.elsevier.com/locate/coastaleng

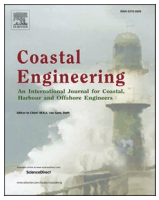

Wave-driven hydrodynamics around a saltmarsh cliff under storm conditions: the role of cliff height and vegetation

J.R.M. Muller [a,*], B.W. Borsje [a], J.J. van der Werf [a,b], D. Dermentzoglou [c], B. Hofland [c], A. Antonini [c], S.J.M.H. Hulscher [a]

[a] University of Twente, Water Engineering and Management, P.O. Box 217, 7500 AE, Enschede, the Netherlands
[b] Deltares, Marine & Coastal Systems, P.O. Box 177, 2600 MH, Delft, the Netherlands
[c] Delft University of Technology, Civil Engineering and Geosciences, P.O. Box 5048, 2600 GA, Delft, the Netherlands

ARTICLE INFO

Keywords:
Saltmarsh
Cliff
Vegetation
PIV
Nature-based solution
Coastal protection
Storm conditions

ABSTRACT

Saltmarshes are a promising nature-based alternative for conventional flood protection. However, saltmarshes can erode under storm conditions, whereby the seaward edge of the saltmarsh often forms a vertical cliff. Despite its importance, the effect of storm conditions on erosion at the saltmarsh cliff remains understudied, especially when waves traverse over a cliff. This research investigates the complex flow patterns around a saltmarsh cliff non-intrusively using Particle Image Velocimetry (PIV) conducted through a series of scaled monochromatic wave flume experiments. We adopted realistic foreshore configurations (e.g. cliff heights) and hydraulic loading conditions from the Dutch Wadden Sea. Results show two local near-bed velocity maxima on top of the saltmarsh, created during different wave phases by water depth contraction, wave transmission and interaction between flow and vortices that are shed from the cliff. Under the wave crest, high onshore-directed near-bed velocities were measured at approximately 2.5–4 times the cliff height onshore from the cliff. Under the wave trough, high offshore-directed velocities were found at the marsh edge. Both onshore- and offshore-directed velocities increase with increasing cliff height, larger wave height or lower water depth. Vegetation on top of the marsh reduces both the incoming and outgoing velocities in front of the cliff. Increasing the cliff height resulted in a greater reduction in velocities by the vegetation. These results demonstrate how local near-bed velocity maxima and location are influenced by the presence of a cliff and the interaction with vegetation on top of the saltmarsh. This research highlights the vulnerability of the cliff even during inundation of the cliff and will help to implement saltmarshes as nature-based solutions for flood defence.

1. Introduction

Rising sea levels and a higher frequency of storms cause an increased pressure on coastal regions and communities (Lee and Marotzke, 2021). Populations residing in coastal areas face growing risks from coastal flooding, with projections indicating a significant rise in associated damages (Edmonds et al., 2020; Neumann et al., 2015). Given the increasing pressure and number of people affected, coastal protection needs to be constructed or updated globally (Nicholls et al., 2010). Over recent decades, it has become more accepted to consider 'hybrid' coastal defence strategies to reinforce coastal protection through Nature-based Solutions (NbS) rather than relying solely on hard infrastructure, e.g. asphalt-covered dikes (Borsje et al., 2011; Doody, 1992; Sutton-Grier et al., 2015; van Wesenbeeck et al., 2014).

A benchmark example of such a hybrid solution is the use of coastal wetlands, e.g. saltmarshes in combination with existing coastal sea dikes (Reed et al., 2018; Temmerman et al., 2013). These types of ecosystems mainly occur on barrier coasts and estuaries in temperate climates (Allen, 2000; Mcowen et al., 2017) and exist between the high and low mean water level where saline vegetation is able to grow (Visser et al., 2019; Willemsen et al., 2018). Numerous studies have demonstrated the ability of vegetation to attenuate wave energy under mild conditions (French, 2019; Gedan et al., 2011). Even during storm conditions (i.e. high inundation levels and large waves), wave energy is still attenuated, despite the large water depth above the saltmarsh (Möller et al., 2014). As a consequence, wave-driven run-up and overtopping is reduced at coastal dikes with a saltmarsh in front of it, making it an interesting alternative investment compared to the necessary heightening and

* Corresponding author.
E-mail address: j.r.m.muller@utwente.nl (J.R.M. Muller).

https://doi.org/10.1016/j.coastaleng.2025.104875
Received 10 April 2025; Received in revised form 7 August 2025; Accepted 6 September 2025
Available online 8 September 2025

widening of sea dikes with no saltmarsh in front (Baker et al., 2022; Costanza et al., 1989; Marin-Diaz et al., 2023; Vuik, 2019; Vuik et al., 2016). Moreover, attenuation of wave energy creates calm conditions on the saltmarsh, effectively capturing sediments (Stark et al., 2015). With an adequate supply of sediment, a saltmarsh can adapt to rising sea levels, reducing the impact of higher wave energy on coastal structures (Kirwan et al., 2016; Mariotti and Fagherazzi, 2010). The presence of vegetation also strengthens the saltmarsh substrate, making it more resistant to erosion through root structures (Chirol et al., 2021; van Eerdt, 1985), higher rates of consolidation (Stoorvogel et al., 2024) and indirect modification of soil parameters (Evans et al., 2022; Feagin et al., 2009). Moreover, saltmarshes provide multiple relevant ecosystem services, such as highly effective sequestration of carbon stocks (Chmura et al., 2003; Duarte et al., 2013), vital habitat for multiple coastal flora and fauna (Adam, 1990; Barbier et al., 2011) and other socio-economic benefits, such as recreation (Beaumont et al., 2008).

Despite the significant advancements in fundamental understanding of the functioning of saltmarsh systems, still many uncertainties remain before implementing saltmarshes as NbS for flood protection. As wave attenuation and other ecosystem services scale with the spatial extent of the marsh, the marsh needs to remain within certain spatial limits for the desired lifetime of the coastal protection. However, saltmarshes are dynamic systems, varying in extent over time. Progradation and retreat follow each other in a cyclic pattern through various feedback mechanisms between hydrodynamic forcings, vegetation establishment and morphodynamical adaption (Allen, 1989; Dzimballa et al., 2024; Fagherazzi et al., 2013; van de Koppel et al., 2005; Willemsen et al., 2022). Global change in hydrodynamic forcing led to rapid saltmarsh erosion worldwide (Evans et al., 2021; Mariotti and Fagherazzi, 2013). In fact, saltmarshes have one of the highest deterioration rates compared to other ecosystems (Millennium Ecosystem Assessment, 2005). Lateral erosion of the marsh edge occurs due to the difference in erosion resistance between the bare mudflat and the saltmarsh (Bouma et al., 2016; Cao et al., 2021; Willemsen et al., 2018). This results in the formation of a step or cliff at the marsh edge (Fig. 1), with heights which can range between 0.2 and 1 m in height with many examples worldwide (Allen, 2000; Bendoni et al., 2016; van der Wal et al., 2023; Wang et al., 2017). Once a cliff is formed, it dictates lateral erosion rates due to the interaction of wave- and current-driven hydrodynamics and substrate characteristics at the cliff (Bouma et al., 2016; van Eerdt, 1985; Wang et al., 2017). Thereby it directly determines the length of the saltmarsh and its wave attenuation capacity. Often, a relationship is found between incoming wave power and the spatial-temporal-averaged loss rate of the marsh (Finotello et al., 2020; Leonardi et al., 2016; Marani et al., 2011). However, this relation can not be generalized as it is neither consistently linear nor uniform, being highly dependent on specific site conditions (Houttuijn Bloemendaal et al., 2023).

Wave-driven erosion mechanisms of a saltmarsh cliff depend on the water level in front of the cliff, e.g. local tidal range, and wind or wave-driven setup (Tonelli et al., 2010; Valentine and Mariotti, 2019; Visser et al., 2019; WinklerPrins et al., 2024). When water levels remain below the top of the cliff during a storm, wave energy predominantly impacts the cliff directly, leading to mass erosion through undercutting and eventual failure by toppling (Tonelli et al., 2010; Francalanci et al., 2013; Bendoni et al., 2014). This process is further facilitated by the variations in soil strength between the upper and lower layers due to the presence of roots in the upper portion of the cliff (Bendoni et al., 2016; Brooks et al., 2022; van Eerdt, 1985). In a macro-tidal system or during larger storms, the coexistence of storm surge, high tidal elevation and wave-driven setup led to large water depths on top of the marsh and bigger waves are able to reach the marsh. Rather than to impact the cliff directly, they traverse over the marsh instead (Fagherazzi, 2014). During these conditions, complex hydrodynamics and accelerations emerge around the stepped saltmarsh cliff (Suzuki and Klaassen, 2011). Strong gradients in horizontal velocities lead to high near-bed stresses, potentially leading to local scour at the cliff (Cadigan et al., 2023; Karimpour et al., 2016). Field observations describe vegetation being removed from the top of the cliff, including below-ground biomass (Cahoon, 2006). This removal leaves the soil more exposed without root systems making it more vulnerable to erosion (Trosclair, 2013). While some research has been carried out on wave-driven flow interaction with a cliff (Huang and Dong, 2001; Suzuki and Klaassen, 2011), the near-cliff velocities have not yet been quantified. The complex near-cliff flow structures are initiated by the cliff leading to the hypothesis that these near-bed velocities scale with cliff dimension and wave characteristics. Moreover, the impact of vegetation at the saltmarsh cliff on these velocities, as well as the effects of vegetation removal during storms, remain unclear. This paper aims to quantify the wave-driven near-bed velocities on top of a saltmarsh cliff and determine the role of vegetation on these flow patterns during storm conditions.

Fig. 1. Saltmarsh in front of a sea dike at Wierum, the Netherlands including an eroding cliff with a height of 0.6 m at the marsh edge of the ca. 100 m long saltmarsh. The sea dike behind the marsh is the main coastal protection structure. (courtesy S. Dzimballa, picture taken November 2022).

2. Methodology

2.1. Scaled wave flume setup

Physical experiments are conducted in the 40.0 m long, 0.8 m wide and 1.0 m high wave flume at the Hydraulic Engineering Laboratory of Delft University of Technology. The flume is equipped with a piston-type wave generator featuring Active Reflection Compensation (ARC). The physical model consists of a foreshore, a saltmarsh and a dike (Fig. 2). Froude similitude (1:10) is adopted for the scaling of the model. The dimensions of the physical model as well as the wave conditions are based on typical Dutch Wadden Sea saltmarshes. The foreshore consists of a 1:9 and 1:45 slope to ensure realistic and gradual wave shoaling up to the edge of the saltmarsh. While natural mudflats can have even gentler slopes, typically between 1:750 and 1:1,000 (Colosimo et al., 2020; Vuik et al., 2016), a steeper slope is necessary in the model due to the limited length of the flume. Coated plywood is used as the construction material to replicate the hydraulic smoothness of a bare mudflat as accurately as possible. The saltmarsh is modelled as a smooth, 7 m long, flat platform and was tested with and without artificial vegetation. Saltmarshes along the Dutch Wadden Sea coast can range from 0 to 1,000 m in width (Zhu et al., 2020). The model marsh was scaled down due to the limited length of the flume, while still maintaining sufficient distance between the marsh edge and the dike. The marsh platform can be raised to reproduce a straight cliff at the transition between foreshore and saltmarsh with different cliff heights, h_c. The physical model replicates a recently eroded cliff, which often show a nearly vertical step (Möller and Spencer, 2002). A total of 3 cliff configurations are made: no cliff, $h_c = 0.06$ m and $h_c = 0.12$ m. As such, a total of 6 model setups (Table 1) are tested for the offshore regular wave conditions. The water depth on the saltmarsh, d_m is defined as the difference between the offshore water depth (d_0) and the height of the foreshore (0.24 m) and the cliff height (h_c) when present. When a cliff is included and the marsh is raised, the marsh is extended at the end to connect to the dike slope. Finally, a dike is included with a slope of 1:3.6 at the end of the saltmarsh.

The targeted vegetation is *Spartina Alterniflora*, or smooth cordgrass. An overview of representative values for *Spartina Alterniflora* is reported by Zhang et al. (2022). The vegetation is modelled by cylindrical neoprene cord, which is cut and glued on a smooth base in a sparse grid with diagonal alignment to create a meadow (Fig. 2). A total of 45,200 stems were placed, giving the meadow a density of approximately 8,100 stems/m^2. The target saltmarsh meadow is chosen with a density N of 190 shoots/m^2, a stem height l_v of 0.9 m, a stem diameter D of 8.5 mm, a stem elastic modulus E of 1,000 MPa and a plant material density ρv of 840 kg/m^3, which is in the lower range measured by Zhang and Nepf (2021). These values correspond to the fully grown state, which is to be expected at the start of the storm season.

Table 1
Physical model setup configurations depending on cliff height (h_c) and presence (✓) or absence (×) of vegetation.

Setup ID	h_c [m]	vegetation
SU1	0	×
SU2	0.06	×
SU3	0.12	×
SU4	0	✓
SU5	0.06	✓
SU6	0.12	✓

The vegetation properties were scaled according to Luhar and Nepf (2016), which discusses 3 dimensionless numbers governing the blade motion within an oscillating flow, namely the Cauchy number Ca, the buoyancy number B and the ratio of the stem length and the wave excursion L:

$$Ca = \frac{\rho D U_w^2 l_v^3}{EI} \quad \text{Eq. 2.1}$$

$$B = \frac{(\rho - \rho_v) g D^2 l_v^3}{4EI} \quad \text{Eq. 2.2}$$

$$L = \frac{l_v \omega}{U_w} \quad \text{Eq. 2.3}$$

With ρ the density of water at 20 °C and g the gravitational acceleration (= 9.81 m/s^2). U_w is the horizontal oscillatory velocity as a representative velocity scale for interacting with the vegetation (Méndez et al., 1999). Here it is determined by Airy wave theory just at the saltmarsh edge at the top of the vegetation. For all non-broken wave conditions, U_w

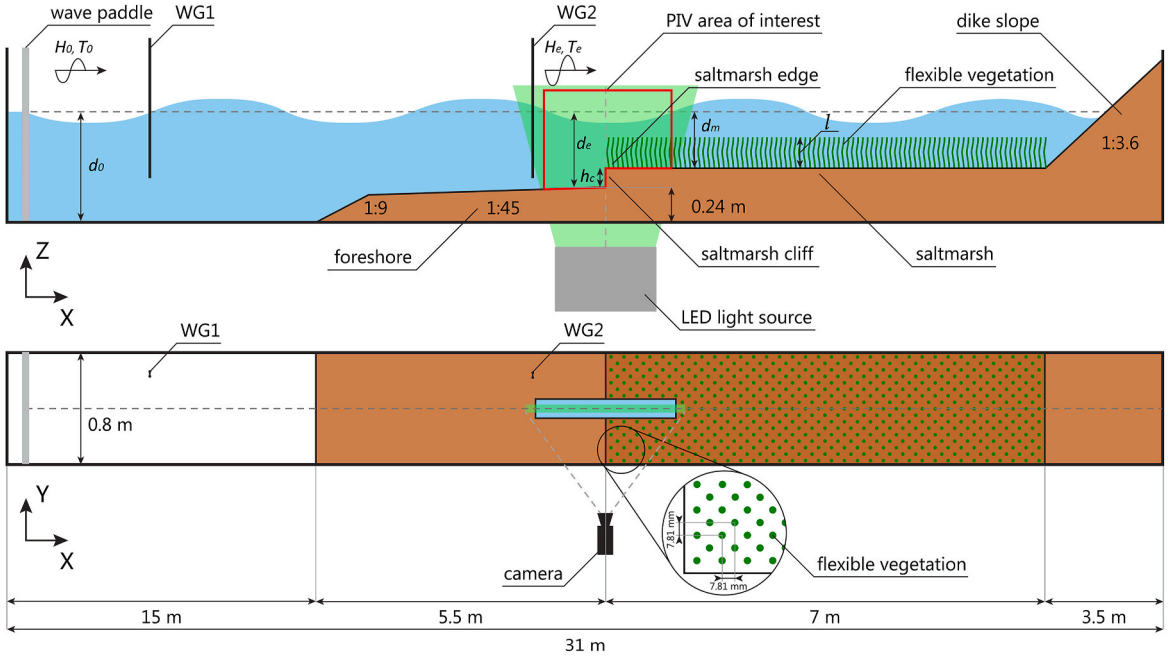

Fig. 2. Schematic overview of the physical model setup, dimensions and measuring equipment.

varies between 0.2 and 0.5 m/s, during which similarity of the above described dimensionless numbers is maintained. A value of $U_w = 0.5$ m/s is used for the scaling procedure (Table 2). Initial scaling of with above scaling laws lead to low vegetation Reynolds numbers for less energetic wave scenarios (e.g. R16, Table A1, $U_w = 0.2$ m/s and $Re_v < 150$). Wave-induced flow interaction with vegetation show vortex shedding causing turbulent wakes at $Re_v > 200$ (Nepf, 1999). Typical Re_v for *Spartina Alterniflora* in field conditions are $Re_v \approx (1000)$ (Jadhav, 2012). To account for this scaling effect, the width of the stem was increased to $D = 2$ mm. The total drag force by the meadow was maintained by decreasing the density of the stems according to:

$$N_1 F_{D,1} = N_2 F_{D,2} \quad \text{Eq. 2.4}$$

Where F_D the drag force, calculated as $\frac{1}{2}\rho C_D D l U_w{}^2$, with C_D the drag force exerted by the meadow. The subscript 1 and 2 is indicating the meadow before and after combining shoots respectively. The appropriate meadow density is then calculated as:

$$N_2 = N_1 \frac{D_1}{D_2} \quad \text{Eq. 2.5}$$

The final modelled saltmarsh meadow maintained Cauchy similitude (Table 2). Buoyancy for both the prototype and the model is small and similitude is maintained with $B < 1$. As discussed by Luhar and Nepf (2016), buoyancy is of lesser importance in oscillatory flow as $CaL > B$. The length ratio is fulfilled due to Froude scaling with $L > 1$ for most of the wave conditions.

The experimental test program consists of series of monochromatic wave scenarios for a total of 6 model setups (Table A1). The first set of wave scenarios are carried out for each setup, varying in offshore water depth d_0, offshore wave height H_0 and offshore wave period T_0, with the offshore wave steepness, s_0 roughly at $s_0 = 0.04$ (R01 – R20, Table A1). Wave conditions are based on severe to extreme storm conditions that apply for the Dutch Wadden Sea coast. Typical for this location, design conditions consist of significant wave height of $H_{m0} = 1.8$ m, $T_{m\text{-}1,0} = 5$ s and marsh inundation of 3 to 4 m (Vuik et al., 2016) and corresponds to similar extreme values of wave conditions for the Dutch Wadden Sea coast (Lavidas and Polinder, 2019).

Additionally, 9 scenarios are carried out for the setup with the highest cliff $h_c = 0.12$ m, with and without vegetation (e.g. SU3 and SU6 respectively), where either the wave height, wave period or water depth is varied (R21 – R29, Table A1). Measured velocities by Particle Image Velocimetry (PIV) are compared to measurements by Acoustic Doppler Velocimeter (ADV) for 3 specific scenarios (R30 – R32, Table A1), including with and without a cliff (e.g. SU1 and SU3 respectively) and no cliff with vegetation (SU4), which are representative for whole set. Broken waves prior to entering the area of interest are excluded from the analysis by applying the Miche breaker criterion. Secondly, wave breaking within the area of interest is visually inspected and these cases are excluded from analysis.

Table 2
Prototype and model values of target vegetation Spartina Alterniflora (smooth cordgrass).

		Unit	prototype	model
elastic modulus	E	Mpa	$1x10^3$	8
vegetation density	ρ_v	kgm^{-3}	840	1,230
density of water	ρ	kgm^{-3}	1,010	1,000
stem length	l_v	m	0.900	0.090
stem density	N	m^{-2}	190	8,550
stem diameter	D	m	0.009	0.002
velocity scale	U_w	ms^{-1}	1.7	0.5
angular frequency	ω	s^{-1}	1.2	4.0
Cauchy number	Ca	–	58	65
Buoyancy number	B	–	0.2	−0.8
Length ratio	L	–	0.7	0.7
vegetation Reynolds number	Re_v	–	15,084	1,060

2.2. Measurements

The complex wave-driven flow around the cliff is measured non-intrusively using Particle Image Velocimetry (PIV). The area of interest consists of a 2DV plane in the middle of the flume around the salt-marsh edge. The total area of view spans around 0.6 m in the horizontal x-direction and 0.7 m in the vertical z-direction. An in-house-developed LED-based line light is chosen as the light source, due to its ease of use and sufficient strength of the light sheet (Bakker et al., 2021). To avoid wave breaking disrupting the illumination of the water column in front of the cliff, the light sheet is emitted from below the flume through a glass section at the bottom of the flume. A transparent plastic window in the physical model allows the light to illuminate the water column. In case of vegetation, two rows of vegetation are removed for the light to pass through the saltmarsh meadow. The light sheet is positioned so that the focal point is in the centre of the area of interest, where the light sheet has a width of 6 mm. The water is seeded with near-neutrally buoyant, polyamide spheres, with a diameter of 100 μm and a density of 1,060 kg/m^3. A camera (ORX-10G-51S5M-C) is mounted perpendicular to the flume, with the principal point aligned with the marsh elevation. The distance between the camera and the centre of the light sheet is 1.16 m. The camera captures images of 2048 × 2448 pixels at 40 Hz. The interrogation window is set at 32 × 32 pixels with a 50 % overlap. This setup results in both horizontal and vertical resolution of 0.3 mm/pixel, corresponding to a single velocity measurement for an area of around 4.4 mm^2. The camera and light pulse are synchronized to capture pairwise images according to the frame straddling technique with a delay of 4.2 ms between each illuminated image. The corresponding velocity resolution is 7 mm/s, using a typical displacement bias of 0.1 px (Westerweel, 1997). The potential for peak-locking is assessed by verifying that the measured particle displacement does not approximate an integer value. The amount of particles per interrogation window is set to be more than 10 particles per interrogation window (Adrian, 1991). A cross-correlation analysis is conducted on pairwise frames, generating two-dimensional velocity fields (x, z) using the PIVLAB toolbox (Thielicke and Sonntag, 2021). Outliers were removed using a standard deviation filter ($n = 8$).

Water surface elevation is measured by resistance-type wave gauges with a frequency of 100 Hz at an offshore location (WG1, 6.4 m onshore from the wave paddle) and just before the marsh edge (WG2, 0.3 m before the marsh edge, just outside view from the camera, Fig. 2). The presence of a cliff leads to wave reflection, which becomes stronger as the water depth on the cliff decreases (e.g. Dean and Dalrymple, 1991). To mitigate this effect, the wave height measured at the saltmarsh edge H_e (WG2, Fig. 2) for the case without a cliff (SU1) is used as the incoming wave for the cases with a cliff (SU2 & SU3). The uncertainty in determining the incoming wave height is small, as the foreshore is unchanged between setups and the offshore wave heights and periods generated show high consistency in between setups, with mean differences of less than 1 %. The transmitted wave height over the cliff is calculated as follows:

$$H_T = K_T \cdot H_e \quad \text{Eq. 2.6}$$

With K_T, the wave transmission coefficient, which is based on the formulation by Dean and Dalrymple (1991):

$$K_T = \frac{2}{1 + \sqrt{\frac{d_m}{d_e}}} \quad \text{Eq. 2.7}$$

To ensure that the reflected waves from the dike do not affect the velocities at the marsh edge and to exclude the spin up time of the wave generator, only the first 10 fully developed waves are analysed. The water particle velocities are verified to follow a repeatable cycle, confirming that the selected 10 waves are sufficient.

To gain trust in the PIV velocity measurements, velocities obtained from PIV are compared against those recorded by an Acoustic Doppler

Velocimeter (ADV) for 3 different setups (R30-R32, Table A1). Scenarios are repeated multiple times with the ADV positioned at different locations around the marsh edge (Fig. 3). The ADV operates at a sampling frequency of 200 Hz for a duration of 40 fully developed waves. The sample volume height is 4 mm and a roughly fixed width similar to the diameter of the transmitted pulse, which is ca. 6 mm (Lohrmann et al., 1994). Low-quality data are filtered based on Signal-to-Noise Ratio (SNR) and correlation. SNR, expressed in decibels, represents the ratio of signal strength to background noise, while correlation measures the consistency of the received acoustic signal, with higher values (typically > 70 %) indicating more reliable data. Data are removed if SNR falls below 15 dB or if correlation is less than 60 % (Nortek AS, 2018). Additional outliers in the ADV measurements are identified and removed when the residual time series, calculated as the difference between the measured time series and a continuous moving median (with a 0.4 s time window), exceeds twice the standard deviation. To minimize the influence of turbulence, phase-averaged horizontal and vertical velocities from both PIV and ADV datasets, are compared for each location. The degree of agreement between PIV and ADV-derived measurements is quantified using the relative root mean square error (RRMSE), which is computed separately for the horizontal and vertical velocity components across all measurement locations as follows:

$$RRMSE = \sqrt{\frac{\frac{1}{N}\sum_{i=1}^{N}(y_i - \hat{y}_i)^2}{\sum_{i=1}^{N}(\hat{y}_i)^2}} \quad \text{Eq. 2.8}$$

where y and $\hat{y}$ is either horizontal or vertical velocity component measured by ADV or PIV respectively, i is the location and N is the total number of data points.

Vortex generation is identified through the swirl strength λ_{ci}, which is the imaginary part of the complex eigenvalue of the velocity gradient tensor (Jeong and Hussain, 1995; Zhou et al., 1999). The swirl strength physical interpretation can be seen as the frequency of the fluid particle to swirl around the centre of a vortex, with the swirl strength dimension in s^{-1}. Compared to vorticity, the swirl strength is less affected by shear layers (Chen et al., 2014). The swirl strength is calculated as:

$$\lambda_{ci}^2 = -4\frac{\partial u}{\partial z}\frac{\partial w}{\partial x} + 2\frac{\partial u}{\partial x}\frac{\partial w}{\partial z} + \frac{\partial u^2}{\partial x} + \frac{\partial w^2}{\partial z} \quad \text{Eq. 2.9}$$

With u and w, the horizontal and vertical velocity component, respectively. The swirl strength is made dimensionless (λ'_{ci}) in a similar way as Lin and Huang (2010), using the cliff height h_c as a characteristic length scale:

$$\lambda'_{ci} = \frac{\lambda_{ci} h_c}{\sqrt{g d_e}} \quad \text{Eq. 2.10}$$

To gain more insight in the maximum near-bed velocities, the horizontal velocity component is extracted at the marsh edge till 0.3 m onshore ($0 < x < 0.3$ m, with x = 0 defined at the marsh edge) at a height ranging from 5 mm, which is the height of one interrogation window to 10 cm from the bed ($0.005 < z < 0.1$ m, with $z = 0$ defined at the bed of the marsh). The maximum onshore- and offshore-directed horizontal velocity are quantified as the 95th and 5th percentile (u^+ and u^- respectively) over the full time series of 10 waves. Finally, u^+ and u^- are made dimensionless using a characteristic velocity scale $\sqrt{g d_e}$:

$$U^+ = \frac{u^+}{\sqrt{g d_e}} \text{ and } U^- = \frac{u^-}{\sqrt{g d_e}} \quad \text{Eq. 2.11}$$

Where U^+ and U^- are the nondimensional maximum onshore and offshore-directed velocity respectively.

Next, the influence of vegetation on the flow velocities at the marsh edge is examined. Due to the visual obstruction by the vegetation, velocity measurements within the canopy are not possible. Additionally, the swaying of vegetation introduces noise in the PIV measurements. Therefore, horizontal phase-averaged velocities $\langle u \rangle$ are extracted along a vertical profile, 20 mm in front of the marsh edge, for both vegetated and non-vegetated scenarios, which are varying over height of the profile and time. The vertical profile covers the water depth above the marsh (d_m) under both onshore and offshore-directed flow, defined as still water depth minus wave amplitude during offshore flow and still water depth plus wave amplitude during onshore flow. Next, the maximum and minimum phase-averaged horizontal velocities (i.e. onshore- and offshore-directed respectively) were computed for each height on the vertical profile, denoted as $\langle u \rangle_v^+$ and $\langle u \rangle_v^-$ for the vegetated case and $\langle u \rangle^+$ and $\langle u \rangle^-$ for the non-vegetated case, which vary over z. The influence of vegetation is quantified by calculating the absolute

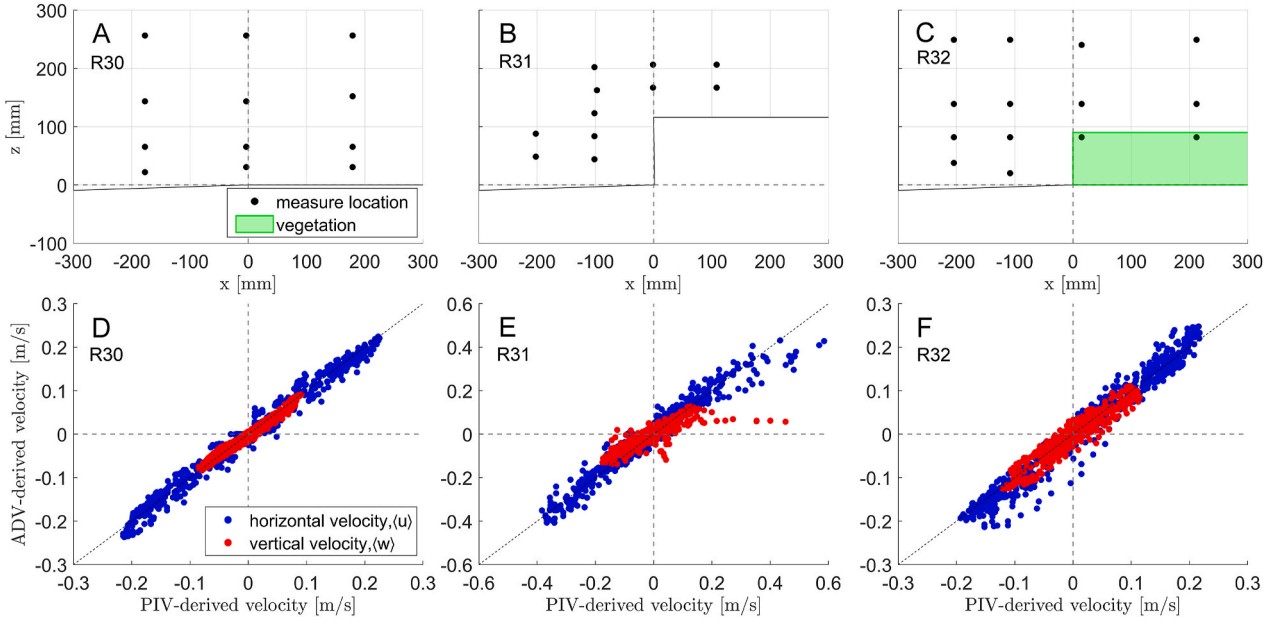

Fig. 3. Comparison between the ADV and PIV measurements for 3 setups; R30, R31 and R32. Top panels show the sampling locations of ADV and PIV (A, B, C, black dots). Lower panels show the comparison between ADV- and PIV-derived horizontal (blue dots) and vertical velocities (red dots) (D, E and F). (For interpretation of the references to colour in this figure legend, the reader is referred to the Web version of this article.)

difference of the non-vegetated and vegetated velocity profiles (i.e. $|\langle u\rangle - \langle u\rangle_v|$), where a value larger than zero means attenuation by vegetation. The reduction of velocity due to the presence on the vegetation is averaged from the bed of the marsh to the height of the standing vegetation and normalized by the characteristic velocity scale $\sqrt{gd_e}$, expressed as ΔU_v^{*+} and ΔU_v^{*-} for onshore and offshore velocities, respectively:

$$\Delta U_v^{*+} = \frac{1}{l\sqrt{gd_e}} \int_0^l \left|\langle u\rangle^+ - \langle u\rangle_v^+\right| dz \qquad \text{Eq. 2.12}$$

$$\Delta U_v^{*-} = \frac{1}{l\sqrt{gd_e}} \int_0^l \left|\langle u\rangle^- - \langle u\rangle_v^-\right| dz \qquad \text{Eq. 2.13}$$

3. Results

3.1. ADV and PIV comparison around the marsh edge

Horizontal and vertical velocities measured by ADV and PIV are compared for three setups, showing good agreement in all cases. First, without a cliff and vegetation (R30, Fig. 3A–D), both velocity components have RRMSE below 1 % of the orbital amplitude measured by PIV for all 12 locations. For the case with a cliff of h_c = 0.12 m (R31, Fig. 3B–E), more scatter is observed, but RRMSE remains around 1–2 % for 11 locations. For the case without a cliff with vegetation (R32, Fig. 3C–F) measurements align well, with both horizontal and vertical velocities for 14 locations again showing RRMSE below 1 % of the measured orbital amplitude measured by PIV.

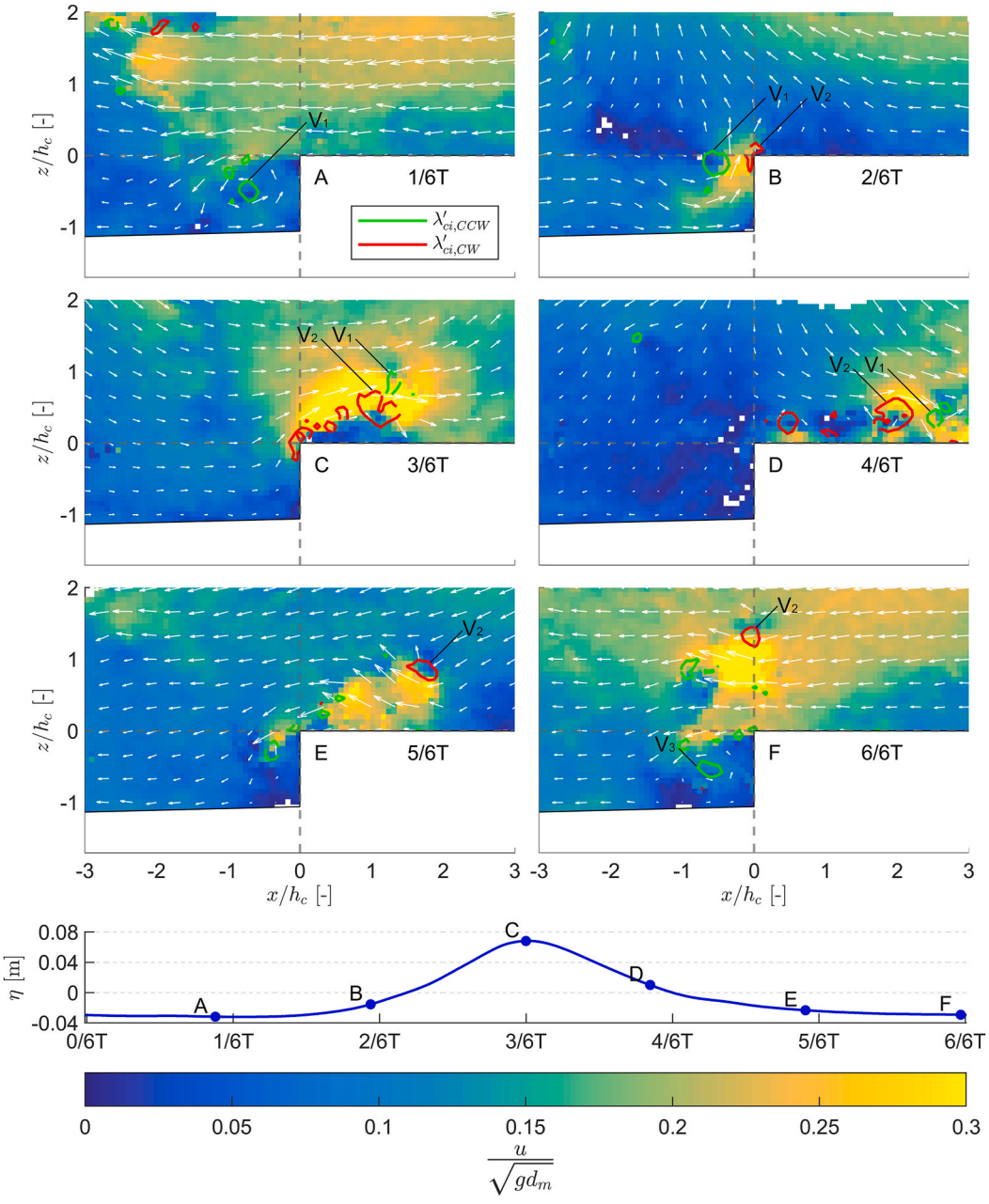

Fig. 4. Instantaneous dimensionless velocities (A–F) during different phases of the wave at $x/h_c = 0$ (lower panel) for a single representative experiment (R09, H_0 = 0.10 m, T_0 = 1.4 s, d_0 = 0.45 m, d_m = 0.15 m, h_c = 0.06 m and no vegetation). Vortices are indicated by dimensionless swirl strength for clockwise (red contours) and counterclockwise (green contours) at λ'_{ci} = 1 [-]. (For interpretation of the references to colour in this figure legend, the reader is referred to the Web version of this article.)

3.2. Velocity patterns around the marsh edge with a cliff

The wave-driven flow patterns over the cliff are analysed for a representative experiment with a 0.06 m high cliff without vegetation and relative large non-breaking waves at the cliff (R09, $H_0 = 0.10$ m, $T_0 = 1.4$ s, $d_0 = 0.45$ m and $d_m = 0.21$ m; Fig. 4). Vortices are identified using the dimensionless swirl strength at a threshold of $\lambda'_{ci} = 1$, based on the dimensionless vorticity observed in a similar experiment (Lin and Huang, 2010). The instantaneous velocities are made dimensionless by a characteristic velocity scale $\sqrt{gd_e}$. To generalize the length scales of the flow patterns, the horizontal length along the marsh and the water depth above it are made dimensionless by the cliff height, expressed as x/h_c and z/h_c, respectively.

Starting at the instance when a wave passed over the cliff, a strong offshore-directed flow is present (Fig. 4A). As the offshore-directed flow cannot follow the abrupt change in local topography, it separates and a counterclockwise vortex develops, indicated by a strong, local swirl strength (V_1, Fig. 4A) with a radius of approximately the height of the cliff. Offshore from the cliff, the flow decelerates.

As an incoming wave approaches the cliff (Fig. 4B), the counterclockwise vortex is advected in the onshore direction, moving over the cliff. As a result, flow accelerates between the vortex and the cliff face. This flow is unable to adapt to the abrupt change in bed level created by the cliff, resulting in flow detachment. A recirculation zone forms with several clockwise vortices at the top of the cliff, including one larger vortex (V_2, Fig. 4B).

During the passing of the wave crest over the cliff, both clockwise and counterclockwise vortices are advected onshore over the top of the cliff (V_1 and V_2, Fig. 4C). Due to the local smaller water depth on top of the cliff, the flow accelerates, while the recirculation zone close to the bed grows in length. The clockwise vortex is forced by the detached flow and grows in intensity. The flow is constrained between the clockwise and counterclockwise vortices, creating a jet-like flow.

When the wave crest has passed the cliff, flow starts to reverse and the clockwise vortex is advected offshore over the marsh platform (V_2, Fig. 4D). The counterclockwise vortex is no longer amplified and gradually dissipates (V_1, Fig. 4D). At the end of the recirculation zone, the flow reattaches to the marsh platform, causing high onshore-directed near-bed velocities during this phase of the wave ($2 < x/h_c < 3$ and $z/h_c = 0$, Fig. 4D).

During flow reversal, the flow is constrained between the marsh platform and the clockwise vortex (V_2, Fig. 4E), which forms a jet that persists under the wave trough, causing high offshore-directed near-bed velocities close to the marsh edge ($0 < x/h_c < 2$ and $z/h_c = 0$, Fig. 4E).

The accelerated offshore-directed jet cannot follow the change in bed level at the cliff and it detaches, forcing a counterclockwise vortex in front of the cliff once more (V_3, Fig. 4F). The offshore-directed jet persists in deeper water for a certain period, possibly induced by undulations of the vortex core in the y direction (perpendicular to the field of view), generating small counterclockwise vortices, while being influenced by the clockwise vortex. As the clockwise vortex gradually dissipates into smaller turbulent motions, the jet weakens and eventually dissipates before the flow reverses under the influence of the incoming wave to repeat the cycle (Fig. 4F).

The observed flow patterns, characterized by the formation of clockwise and counterclockwise vortices and the forcing of high near-bed velocities, were consistently repeated throughout the experiment. These patterns also persisted in experiments with a higher cliff height. Similar vortex generation and high near-bed velocities are observed in the other experiments, although the velocity intensity varied with wave conditions (i.e. wave height and wave period) and water depth on top of the marsh (d_m) as are shown next.

3.3. Near-bed velocities around the marsh edge with a cliff under various hydrodynamic conditions

Both onshore- and offshore-directed near-bed peak velocities (U^+ and U^-, Eq. (2.10)) are compared for changes in wave conditions (i.e. wave height and wave period) and change in water depth for a constant cliff height ($h_c = 0.06$ m). Under onshore-directed flow, the accelerated and detached flow over the cliff is distinctly evident over different experiments. Both the intensity and the length of the detached flow increase with increasing wave height (Fig. 5, bottom to top panels) and decreasing water depth (Fig. 5, right to left). As shown in Fig. 4C, a recirculation zone develops underneath the detached flow over the cliff, which can be recognized by relative low maximum near-bed velocities ($0 < x/h_c < 1$). Behind the recirculation zone, local high near-bed velocities are generated as explained in section 3.2. The magnitude of the maximum onshore near-bed velocities as well as their distance from the marsh edge ($x/h_c = 0$) similarly increases with intensifying wave conditions (i.e. H and T) and decreasing water depth (d_m).

During offshore-directed flow under the trough of the wave, high near-bed velocities are generated near the marsh edge (Figs. 6 and $0 < x/h_c < 2$). Similarly to the onshore-directed near-bed velocities, the maximum offshore near-bed velocities increases with increasing wave conditions (i.e. H and T) (Fig. 6, bottom to top) and decreasing water depths (Fig. 6, left to right). The location of the maximum offshore-directed near-bed velocities occurs near the marsh edge and does not show large variation with wave conditions or water depth. The magnitude of onshore- and offshore-directed maximum near-bed velocity are similar, although the area over which these near-bed velocities occur is larger during onshore conditions.

The maximum onshore- and offshore-directed near-bed velocities (i.e. U^+ and U^- respectively) are retrieved along a horizontal profile at a height of ca. 5 mm above the bed and compared for different wave conditions and water depths (Fig. 7). Two zones of high near-bed velocities can be seen; the first being offshore-directed, located at the marsh edge and the second being onshore-directed at some distance from the marsh edge. Both zones exhibit a local maximum, with the magnitude and location varying between experiments. The maxima of U^+ and U^- over the marsh are defined as the absolute maximum onshore- and offshore-directed near-bed velocities, denoted as U^{*+} and U^{*-}, respectively.

For the first zone, the maximum offshore-directed near-bed velocity U^{*-} increases with increasing wave height and decreases with increasing water depth. The location of this maximum offshore-directed flow depends less on wave height and water depth. This can be understood as the maximum offshore-directed flow occurs as the jet is 'trapped' below the clockwise vortex and the cliff until it is beyond the marsh edge (Fig. 4E). The location of the maximum offshore-directed near-bed velocities is therefore bound to the marsh edge. For all wave conditions and water levels, the location of U^{*-} is between the marsh edge (i.e. $x/h_c = 0$) and $x/h_c = 0.5$ (Fig. 7).

For the second zone, the maximum onshore-directed near-bed velocity U^{*+}, similarly increases with wave height and decreases with increasing water depth. However, the location of the maximum onshore-directed near-bed velocities (x_{on}) migrates further onshore with increasing wave height. More energetic wave conditions (i.e. higher H and T), lead to larger recirculation zones and a longer distance from the cliff where the flow can reattach to the bed. In reverse, an increase in water depth leads to both lower maximum near-bed velocity and its location closer to the marsh edge. The first zone, which is offshore-directed, is typically shorter in length over the top of the cliff compared to the second zone, which is onshore-directed.

3.4. The role of cliff height on near-bed velocities

Given all experiments, we now study the relation between maximum

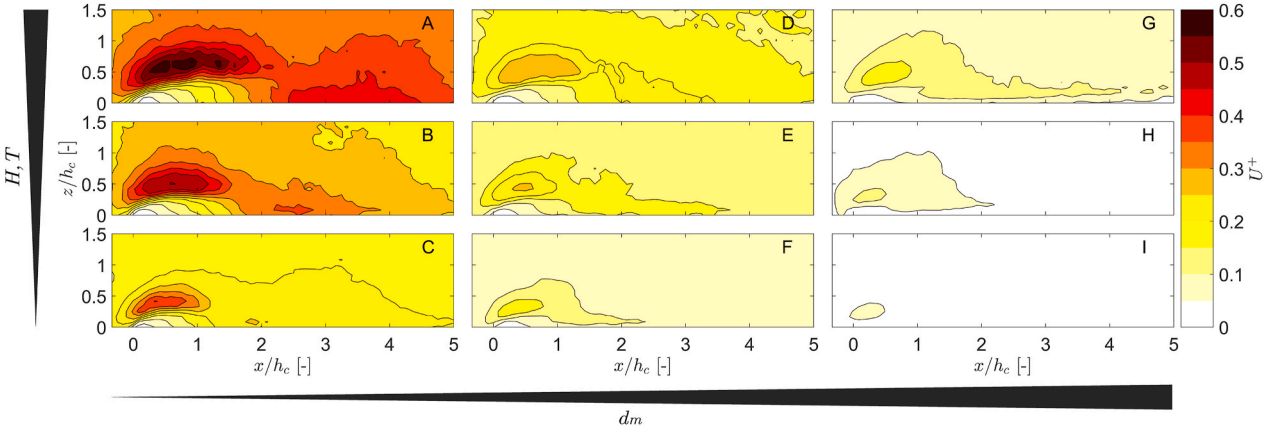

Fig. 5. Onshore-directed maximum horizontal velocity over the marsh platform, U^+ for $h_c = 0.06$ and dependency on an increase in wave height (bottom to top, H_0 = 0.07, 0.08 and 0.10 m) and increase in water depth on top of the marsh (left to right, d_m = 0.15, 0.25 and 0.40 m).

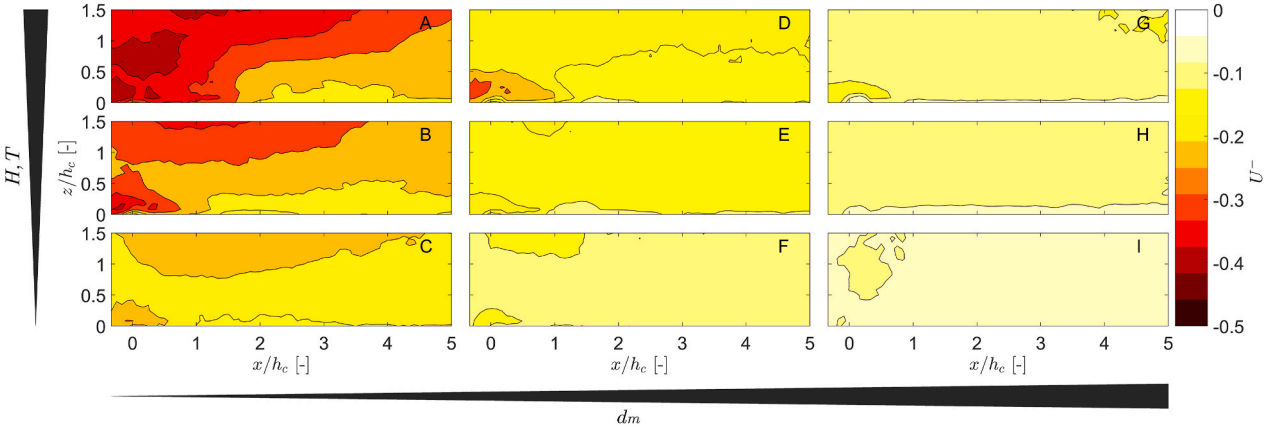

Fig. 6. Offshore-directed maximum horizontal velocity over the marsh platform, U^- for $h_c = 0.06$ and dependency on an increase in wave height (bottom to top, H_0 = 0.07, 0.08 and 0.10 m) and increase in water depth on top of the marsh (left to right, d_m = 0.15, 0.25 and 0.40 m).

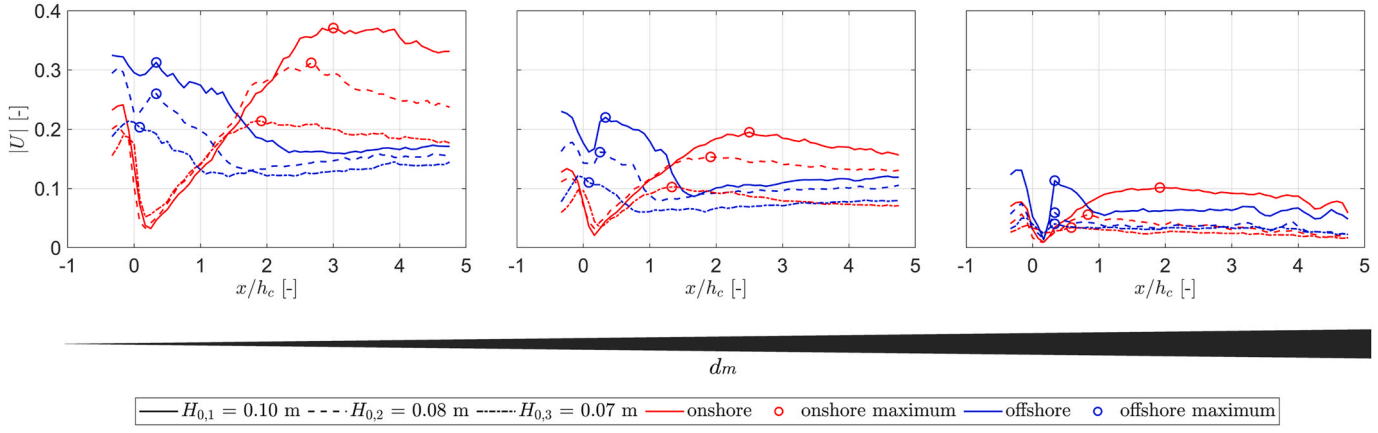

Fig. 7. Maximum absolute near-bed horizontal velocities for onshore- (red line) and offshore-directed flow (blue line) over the saltmarsh at 5 mm above the bed for $h_c = 0.06$ m. The saltmarsh length is made dimensionless by the cliff height. Local maxima in maximum velocities are indicated by open circles. Line styles indicate an increase in offshore wave height (H_0 = 0.07, 0.08 and 0.10 m) and the panels from left to right show an increase in water depth on top of the marsh (d_m = 0.15, 0.25 and 0.40 m). (For interpretation of the references to colour in this figure legend, the reader is referred to the Web version of this article.)

near-bed velocity in both onshore- and offshore-directed flow and the local relative water depth on top of the marsh to the transmitted wave height (d_m/H_T) for three cliff heights (Fig. 8). A clear trend is observed where both U^{*+} and U^{*-} increase with decreasing d_m/H_T. The relation between U^{*+} and d_m/H_T align well across the experiments with and without a cliff, suggesting that near-bed velocity accelerations are primarily governed by the contraction of the water column and the increase in wave height resulting from wave transmission over the cliff. A similar trend is observed for U^{*-}, although at lower d_m/H_T values, the presence of a cliff results in higher U^{*-} compared to the experiments without a

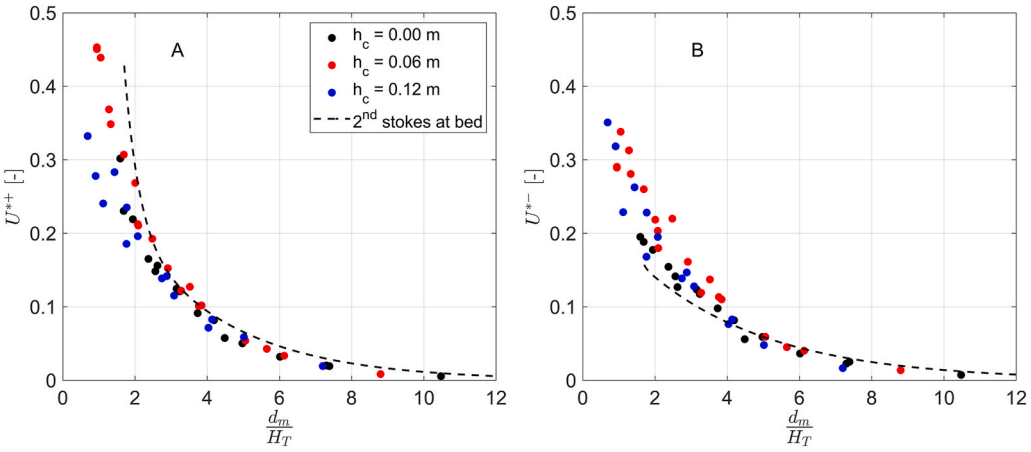

Fig. 8. Relation between relative maximum near-bed velocity and the relative water depth with the transmitted wave height on top of the marsh for both onshore- (A) and offshore-directed flow (B) for various cliff heights ($h_c = 0.06$ m, red dots and $h_c = 0.12$ m, blue dots) and without a cliff (black dots). The data is compared to the near-bed velocity amplitude approximation based second-order Stokes (black dashed line). (For interpretation of the references to colour in this figure legend, the reader is referred to the Web version of this article.)

cliff. This can be attributed to the generation of vortices by the cliff, which accelerate the offshore-directed flow over it. For both U^{*+} and U^{*-}, the influence of different cliff heights is relatively small for the two cliff heights examined in this study.

The near-bed velocities were approximated using second-order Stokes theory (Zhao and Liu, 2022), assuming a constant wave steepness of $s = 0.04$, which is representative of most wave conditions in the experiments (Table A1). Without a cliff, the observations align well with theory. When a cliff is present, good agreement between theory and observed velocities is maintained for larger values of d_m/H_T. However, in shallower conditions, U^{*+} is lower than predicted by theory, while U^{*-} is higher. The later can be explained by the interaction with vortices generated at the cliff, which locally accelerate the offshore-directed flow.

The relationship between the location of the maximum onshore-directed near-bed velocity, x_{on} and the relative water depth on top of the marsh to the transmitted wave height (d_m/H_T) is examined for both cliff heights (Fig. 9). Here, x_{on} is normalized by T_0 multiplied by the characteristic velocity scale. Both cases follow a clear trend where a lower value of d_m/H_T results in an increase in x_{on}. Under the same offshore wave conditions, a higher cliff means a smaller water depth on top of the marsh and a higher transmitted wave height. This causes x_{on} to shift landward, indicating that a larger area on top of the cliff exposed to higher near-bed velocities. This was not found to be directly proportional to the cliff height, where a smaller cliff reaches a maximum distance of $x_{on} \approx 0.25$ m (ca. 4 h_c) and a larger cliff leads to a maximum distance of $x_{on} \approx 0.3$ m (ca. 2.5 h_c).

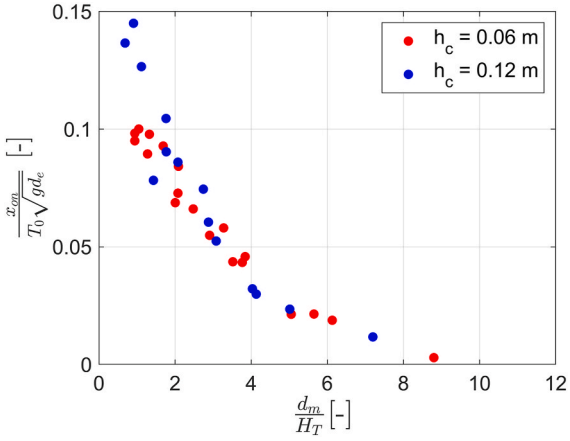

Fig. 9. Relation between the normalized location of maximum onshore-directed near-bed velocity and the relative water depth with the transmitted wave height on top of the marsh for a small ($h_c = 0.06$ m, red dots) and a large cliff height ($h_c = 0.12$ m, blue dots). (For interpretation of the references to colour in this figure legend, the reader is referred to the Web version of this article.)

3.5. The role of vegetation on near-bed velocities

The effect of vegetation on top of a cliff is evaluated by comparing wave-driven velocities just in front of the cliff under the same setups and wave scenarios, both with and without vegetation. Maximum phase-averaged velocities over a vertical profile in front of the saltmarsh are shown for the largest cliff height ($h_c = 0.12$ m), where the effect is most clearly visible (Fig. 10). For both setups (i.e. with and without vegetation), the flow contraction induced by the cliff accelerates the onshore-directed velocity. Vegetation reduces the maximum velocities, particularly in the lower half of the canopy. This is due to bending of the flexible vegetation under the wave forces. In the upper half, the vegetation slightly increases the onshore-directed velocities (e.g. Fig. 10C–G, H) as the flow faces less resistance and is redirected over the vegetation. The drag induced by the vegetation on the onshore-directed flow increases, causes velocities to decrease, with increasing wave height and period (Fig. 10, left to right), and decreases as the water depth increases (Fig. 10, top to bottom panel). A significant reduction in both onshore- and offshore-directed velocities is observed when the water depth above the marsh is similar to the vegetation height ($d_m \approx l_v$). This occurs because, at lower water depths, the flow is forced through the vegetation, while for larger water depths, the flow is redirected over the vegetation.

The combined effect of both the cliff and the interaction with vegetation are compared for both onshore- and offshore-directed flow for each experiment (Fig. 11). The effect of vegetation is expressed through the dimensionless velocity reduction ΔU_v^{*+} and ΔU_v^{*-} (Eq. (2.12) and Eq. (2.13)) for onshore- and offshore-directed maximum, respectively. In the presence of a cliff, both onshore- and offshore-directed velocities show similar pattern, where vegetation decelerated velocities compared to the case without vegetation. An increase in cliff height results in a lower water level and a higher transmitted wave height on top of the cliff. This leads to a decrease in d_m/H_T and corresponds to an increase in both ΔU_v^{*+} and ΔU_v^{*-}. This velocity reduction reaches a maximum of ΔU_v^{*+} and $\Delta U_v^{*-} = 0.05$ for $h_c = 0.06$ m to ΔU_v^{*+} and $\Delta U_v^{*-} = 0.15$ for h_c

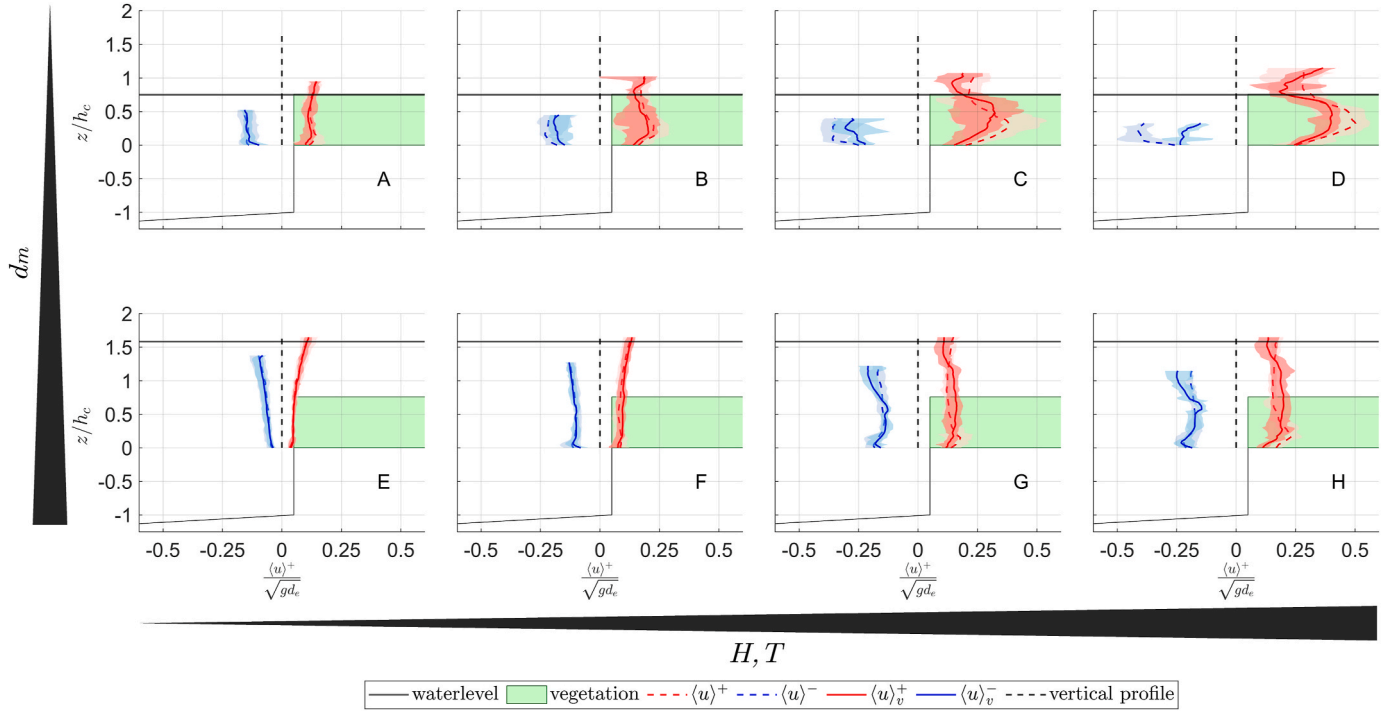

Fig. 10. Maximum onshore-directed (red) and offshore-directed (blue) horizontal velocities, with (solid) and without (dashed) vegetation, along a vertical profile in front of the marsh edge (dashed black line, x = −0.02 m). Still water level is indicated by the solid black line. Panels from left to right show an increase in offshore wave height and period (H_0 = 0.05, 0.07, 0.08 and 0.10 m, and T_0 = 0.9, 1.1, 1.3 and 1.5 s respectively). Panels from top to bottom show increase in water depth (d_m = 0.09 and 0.19 m). (For interpretation of the references to colour in this figure legend, the reader is referred to the Web version of this article.)

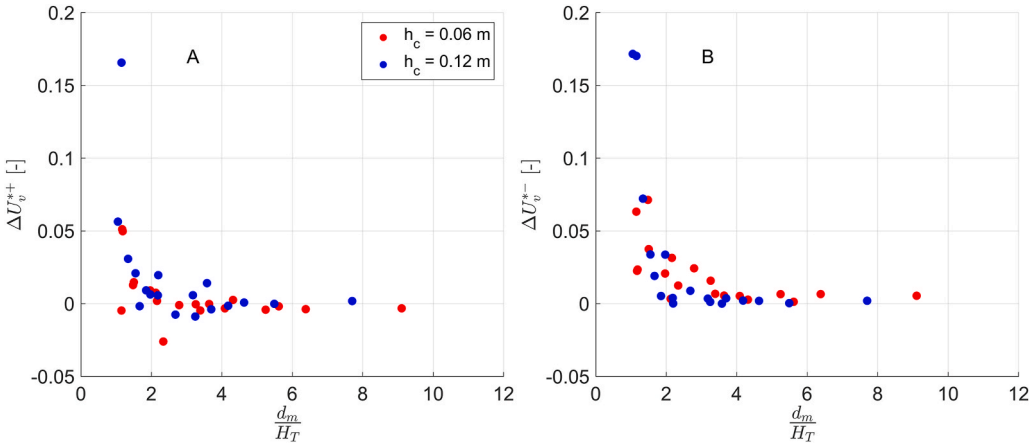

Fig. 11. Relation between dimensionless velocity reduction and the relative water depth with the transmitted wave height on top of the marsh for both onshore- (A) and offshore-directed flow (B) for a small (h_c = 0.06 m, red dots) and a large cliff height (h_c = 0.12 m, blue dots). (For interpretation of the references to colour in this figure legend, the reader is referred to the Web version of this article.)

= 0.12 m. These results demonstrate the vegetation's effectiveness in reducing velocities in front of the vegetation, which increases with cliff height, highlighting the interaction between the cliff and vegetation and is mostly effective at values of $d_m/H_T < 3$.

4. Discussion

4.1. PIV-derived velocity measurements

This study uses 2DV PIV to non-intrusively measure flow patterns across various saltmarsh edge configurations, considering different cliff and vegetation scenarios, wave conditions and water depths. This method provided detailed insights into flow patterns that contribute to high near-bed velocities. A relatively large area of interest enabled the analysis of flow patterns onshore and offshore of the marsh edge. Focusing on a smaller area of interest with higher spatial resolution could enhance the accuracy of near-bed velocity measurements (Lin et al., 2006). However, the results presented here primarily aimed to explain flow behaviour over the whole water column around the marsh edge and relate it to the generation of high near-bed velocities and the effects of a cliff and vegetation on these velocities. It is important to note that only 10 waves were used to determine the phase-averaged velocities to mitigate the effects of dike reflection. While phase-averaging over a larger number of waves would improve the measurement accuracy, the coefficient of variation of the maximum and minimum velocities before the cliff remain ≤ 5 %, indicating that the measured waves

are repeatable.

4.2. Near-bed velocities at a saltmarsh edge

This study shows the generation of high near-bed velocities over the marsh platform, driven by the interaction between wave-driven flow and a cliff during both the wave crest and trough. Similar patterns of vortex generation and advection over submerged rectangular objects have been observed in previous flume studies, particularly under solitary waves (Chang et al., 2005; Lin et al., 2006), where high near-bed velocities are linked to vortex formation and flow detachment (Huang and Dong, 2001; Ting and Kim, 1994). Our findings show that under monochromatic waves, this pattern of clockwise and counterclockwise vortex formation repeats, contributing to the generation of high near-bed velocities.

We present a relationship between velocities on top of the marsh edge and local wave conditions, depending on local water depth and transmitted wave height, though at a constant steepness. Similar dependency was found of vortices size and intensities with depending on wave height and period. Suzuki and Klaassen (2011) also found a dependence of the size and intensity counterclockwise vortex in front of the cliff on wave height and period. Chang et al. (2005) highlighted the interaction between vortices, particularly for shorter wave lengths, where limited dissipation time results in more intense vortices and accelerated near-bed velocities. As with wave-induced pressure on the cliff face, shear stresses are strong when water levels on top of the marsh are low (Tonelli et al., 2010). However, our results demonstrate that when waves are able to traverse the cliff edge, significant shear is exerted on top of the cliff.

The results indicate that high near-bed velocities can develop during storm conditions when the marsh is inundated. These findings are an addition to previous studies on cliff vulnerability under calmer or moderate storm conditions, where wave forces directly impact the cliff, and erosion is primarily driven by direct wave action and substrate composition (Bendoni, 2015; Bendoni et al., 2014; Francalanci et al., 2013). Undercutting of a cliff results in a relatively straight vertical cliff with sharp edges at the top, similar to the modelling of the cliff in this study. During high-energy storm events, these sharp cliffs contribute to flow detachment, repeating the cycle of erosion. Although the generation of vortices and the subsequent high near-bed velocities repeated with every wave cycle, this is not the case under field conditions. During storm conditions, high velocities due to flow contraction over the cliff will gradually smooth the top of the cliff, significantly reducing the separation region and the associated generation of clockwise vortices at the cliff (Rey et al., 1992; Suzuki and Klaassen, 2011).

4.3. Effect of vegetation on near-bed velocities at a cliff

Direct flow measurements inside the canopy were not possible. Instead, the phase-averaged velocities just before the marsh edge were measured, which were not obstructed by vegetation in view of the camera. Results show that vegetation significantly attenuate the flow in front of the marsh edge, reducing flow detachment and vortex generation during both wave phases. Other studies have also found substantial decrease in velocity within the vegetation, albeit without including a cliff at the marsh edge. Karimpour et al. (2016) found that orbital velocity reduction within the vegetation depends on wave height, inundation depth, submergence and the density of the vegetation. In fact, as water depth increases, the vegetations ability to attenuate velocities decreases (Maza et al., 2015; Möller et al., 2014).

It is important to note that the targeted vegetation was fully-grown *Spartina Alteniflora* at the beginning of the storm season. This species is not always present on top of a cliff, particularly when the cliff has been retreating for some time and more high marsh is exposed (e.g. Fig. 1). In such cases, limited vegetation is present due to low inundation frequencies, making conditions more similar to the tested scenarios without vegetation. As such, the results from the experiments with vegetation on top of the marsh offer valuable insights into velocity patterns for newly formed cliffs in retreating salt marshes. In contrast, the non-vegetated experiments are more representative of hydrodynamic conditions around more mature cliffs with small standing vegetation.

4.4. Implications for saltmarsh implementation as nature based solution for flood defence

The results showed that, beyond direct wave impact during smaller or moderate storms conditions with the water level lower than the cliff height, significant wave-driven near-bed velocities occur at the marsh edge when inundated during extreme storm conditions. These high near-bed velocities suggest significant local shear stresses (Huang and Dong, 2001), identifying a hotspot for erosion caused by scour during large inundation.

High hydrodynamic stresses at the cliff can lead to breaking of stiff vegetation (Vuik et al., 2018) or even the uprooting and removal of complete above-ground vegetation and root systems (Cahoon, 2006; Priestas et al., 2015; Temmerman et al., 2023). This exposes the bare substrate, becoming a local weak spot during high over-marsh flow and pressures (Allen, 2000; Marshall, 1962). Hence, these short-term erosion events and vegetation loss could lead to higher lateral erosion rates and collapse of the saltmarsh on longer timescales (Mariotti and Fagherazzi, 2013; Van der Wal et al., 2008).

This implies that coastal managers should consider not only lateral erosion during elevated water levels at the cliff face, but also the increased vulnerability of marsh cliffs during major storm events. This contrasts with earlier findings that reported little to no erosion of the marsh platform itself, even during extreme storm conditions (Brooks et al., 2022; Schoutens et al., 2022; Spencer et al., 2016; van Eerdt, 1985). More intensive monitoring at both the cliff face and the cliff top may help identify active failure mechanisms as they develop. Furthermore, the relationship between over-marsh velocities and local hydrodynamics could serve as a useful indicator of near-bed shear stress acting on top of cliff. Ultimately, the extent of erosion is governed by site-specific soil properties, vegetation characteristics and erosion resistance.

The results show the locations of maximum near-bed velocities under a wide range of storm conditions, which is important information as a first step for the implementation of saltmarshes as nature-based solutions for flood defence. This study highlights the vulnerability of both the cliff and vegetation during storms, emphasizing the need for further research. As a next step, further investigation is recommended in a follow-up study to determine the extent to which these near-bed velocities drive saltmarsh erosion under storm conditions.

5. Conclusion

This study examines wave-driven flow patterns at the marsh edge under storm conditions through a series of wave flume experiments. The role of cliff height and the presence of vegetation on velocities around the marsh edge are examined, with velocities measured non-intrusively using 2DV PIV. The results show the generation of clockwise and counterclockwise vortices as the wave-driven flow cannot follow the sharp transition at the cliff during both onshore- and offshore-directed flow. These vortices are advected, affecting the flow and leading to higher near-bed velocities at different phases of the wave.

The presence of a cliff at the marsh edge lead to the generation of high near-bed velocities either onshore-directed under the crest of the wave or offshore-directed under the trough of the wave. The magnitude of these velocities increases with increasing wave height or decreasing water depth on top of the marsh. Increase in near-bed velocities with increasing cliff height was small for the cliff heights chosen in these experiments. The location of maximum onshore-directed near-bed

velocity depends on the relative water depth and wave height varying between 2.5 and 4 times the cliff height onshore from the marsh edge. In contrast, the maximum offshore-directed velocities consistently occur at the marsh edge.

The presence of vegetation on top of the marsh, in combination with a cliff, shows an attenuation of both onshore- and offshore velocities, potentially mitigating erosion and scour at the cliff, with the effect becoming more pronounced as the cliff height increases and the water depth decreases. These results demonstrate the generation of high near-bed velocities over a saltmarsh cliff when the marsh is submerged under storm conditions. Rather than direct wave impact at low water depths, high near-bed velocities and potential scour on top of the cliff can occur, emphasizing the vulnerability of saltmarsh cliffs under storm conditions. The results identify the locations of maximum near-bed velocities across various storm conditions, cliff heights and presence of vegetation. Thereby providing essential insights as a first step toward implementing saltmarshes as nature-based flood defences. An important next step involves investigating the extent to which these velocities contribute to saltmarsh erosion during storms.

CRediT authorship contribution statement

J.R.M. Muller: Writing – original draft, Methodology, Investigation, Formal analysis, Conceptualization. **B.W. Borsje:** Writing – review & editing, Supervision, Methodology, Formal analysis. **J.J. van der Werf:** Writing – review & editing, Formal analysis. **D. Dermentzoglou:** Writing – review & editing, Investigation. **B. Hofland:** Writing – review & editing, Methodology. **A. Antonini:** Writing – review & editing, Methodology, Formal analysis, Conceptualization. **S.J.M.H. Hulscher:** Writing – review & editing, Supervision.

Declaration of generative AI and AI-assisted technologies in the writing process

During the preparation of this work the author(s) used *ChatGPT-4o* in order to enhance the clarity and coherence of the text. After using this tool/service, the author(s) reviewed and edited the content as needed and take(s) full responsibility for the content of the published article.

Declaration of competing interest

The authors declare that they have no known competing financial interests or personal relationships that could have appeared to influence the work reported in this paper.

Acknowledgements

This work is part of the 'Living Dikes – Realising Resilient and Climate-Proof Coastal Protection' project (NWA.1292.19.257), funded by the Netherlands Organisation for Scientific Research (NWO). The authors want to thank P. van der Gaag, A. Doorn and A. van der Vlies for their contributions to the design and construction of the physical model. Additionally, the support provided during the PIV experiments by W. Bakker, P. Faber, S. Lakerveld C. Willems and F. Kalkman is greatly appreciated. Finally, the valuable contributions of the two anonymous reviewers in improving the draft manuscript are gratefully acknowledged.

Appendices.

A. Experimental program

Table A1
Experimental program with each experiment indicated with an experiment ID, depending on offshore wave height H_0, wave period T_0 and water depth, d_0. Same offshore wave scenarios are repeated for multiple cliff heights h_c and therefore water depth on top of the marsh d_m. Similarly, scenarios were repeated with (✓) and without (×) the presence of vegetation on top of the marsh, with an exemption for experiment R30-R32.

Experiment ID	H_0 [m]	T_0 [s]	d_0 [m]	h_c [m]	d_m [m]	presence vegetation
R01	0.05	0.9	0.40	0, 0.06, 0.12	0.16, 0.10, 0.04	✓/×
R02	0.07	1.1	0.40	0, 0.06, 0.12	0.16, 0.10, 0.04	✓/×
R03	0.09	1.3	0.40	0, 0.06, 0.12	0.16, 0.10, 0.04	✓/×
R04	0.10	1.5	0.40	0, 0.06, 0.12	0.16, 0.10, 0.04	✓/×
R05	0.12	1.7	0.40	0, 0.06, 0.12	0.16, 0.10, 0.04	✓/×
R06	0.05	0.9	0.45	0, 0.06, 0.12	0.21, 0.15, 0.09	✓/×
R07	0.07	1.1	0.45	0, 0.06, 0.12	0.21, 0.15, 0.09	✓/×
R08	0.09	1.2	0.45	0, 0.06, 0.12	0.21, 0.15, 0.09	✓/×
R09	0.10	1.4	0.45	0, 0.06, 0.12	0.21, 0.15, 0.09	✓/×
R10	0.12	1.6	0.45	0, 0.06, 0.12	0.21, 0.15, 0.09	✓/×
R11	0.05	0.8	0.55	0, 0.06, 0.12	0.31, 0.25, 0.19	✓/×
R12	0.07	1.0	0.55	0, 0.06, 0.12	0.31, 0.25, 0.19	✓/×
R13	0.09	1.2	0.55	0, 0.06, 0.12	0.31, 0.25, 0.19	✓/×
R14	0.10	1.3	0.55	0, 0.06, 0.12	0.31, 0.25, 0.19	✓/×
R15	0.12	1.5	0.55	0, 0.06, 0.12	0.31, 0.25, 0.19	✓/×
R16	0.05	0.8	0.70	0, 0.06, 0.12	0.46, 0.40, 0.34	✓/×
R17	0.07	1.0	0.70	0, 0.06, 0.12	0.46, 0.40, 0.34	✓/×
R18	0.08	1.1	0.70	0, 0.06, 0.12	0.46, 0.40, 0.34	✓/×
R19	0.10	1.3	0.70	0, 0.06, 0.12	0.46, 0.40, 0.34	✓/×
R20	0.12	1.4	0.70	0, 0.06, 0.12	0.46, 0.40, 0.34	✓/×
R21	0.10	1.5	0.40	0.12	0.04	✓/×
R22	0.05	1.5	0.45	0.12	0.09	✓/×
R23	0.15	1.5	0.45	0.12	0.09	✓/×
R24	0.10	1.2	0.45	0.12	0.09	✓/×
R25	0.10	2.0	0.45	0.12	0.09	✓/×
R26	0.10	2.5	0.45	0.12	0.09	✓/×
R27	0.10	1.5	0.45	0.12	0.09	✓/×

(*continued on next page*)

Table A1 (*continued*)

Experiment ID	H_0 [m]	T_0 [s]	d_0 [m]	h_c [m]	d_m [m]	presence vegetation
R28	0.10	1.5	0.55	0.12	0.19	✓/×
R29	0.10	1.5	0.70	0.12	0.34	✓/×
R30	0.10	1.6	0.70	0	0.46	×
R31	0.10	1.5	0.55	0.12	0.19	×
R32	0.10	1.3	0.64	0	0.40	✓

Data availability

Data will be made available on request.

References

The saltmarsh biota. In: Adam, P. (Ed.), 1990. Saltmarsh Ecology, Cambridge Studies in Ecology. Cambridge University Press, Cambridge, pp. 72–145. https://doi.org/10.1017/CBO9780511565328.003.

Adrian, R., 1991. Particle-imaging techniques for experimental fluid mechanics. Annu. Rev. Fluid Mech. 23, 261–304. https://doi.org/10.1146/annurev.fl.23.010191.001401.

Allen, J., 2000. Morphodynamics of Holocene salt marshes: a review sketch from the Atlantic and Southern North Sea coasts of Europe. Quat. Sci. Rev. 19, 1155–1231. https://doi.org/10.1016/S0277-3791(99)00034-7.

Allen, J.R.L., 1989. Evolution of salt-marsh cliffs in muddy and sandy systems: a qualitative comparison of British West-Coast estuaries. Earth Surf. Process. Landf. 14, 85–92. https://doi.org/10.1002/esp.3290140108.

Baker, S., Murphy, E., Cornett, A., Knox, P., 2022. Experimental study of wave attenuation across an artificial salt marsh. Front. Built Environ. 8, 893664. https://doi.org/10.3389/fbuil.2022.893664.

Bakker, W., Hofland, B., de Almeida, E., Oldenziel, G., J Overmars, E.F., 2021. Pulsed LED line light for large-scale PIV—Development and use in wave load measurements. Meas. Sci. Technol. 32, 115205. https://doi.org/10.1088/1361-6501/ac17ce.

Barbier, E.B., Hacker, S.D., Kennedy, C., Koch, E.W., Stier, A.C., Silliman, B.R., 2011. The value of estuarine and coastal ecosystem services. Ecol. Monogr. 81, 169–193. https://doi.org/10.1890/10-1510.1.

Beaumont, N.J., Austen, M.C., Mangi, S.C., Townsend, M., 2008. Economic valuation for the conservation of marine biodiversity. Mar. Pollut. Bull. 56, 386–396. https://doi.org/10.1016/j.marpolbul.2007.11.013.

Bendoni, M., 2015. Modelling Bank Erosion of Salt Marshes Inducted by Wind Waves Modulated by Tide. Technical University Braunschweig, University Florence, Braunsweig, Florence. Ph.D. Thesis).

Bendoni, M., Francalanci, S., Cappietti, L., Solari, L., 2014. On salt marshes retreat: experiments and modeling toppling failures induced by wind waves: modeling salt marsh retreat. J. Geophys. Res. Earth Surf. 119, 603–620. https://doi.org/10.1002/2013JF002967.

Bendoni, M., Mel, R., Solari, L., Lanzoni, S., Francalanci, S., Oumeraci, H., 2016. Insights into lateral marsh retreat mechanism through localized field measurements. Water Resour. Res. 52, 1446–1464. https://doi.org/10.1002/2015WR017966.

Borsje, B.W., van Wesenbeeck, B.K., Dekker, F., Paalvast, P., Bouma, T.J., van Katwijk, M.M., de Vries, M.B., 2011. How ecological engineering can serve in coastal protection. Ecol. Eng. 37, 113–122. https://doi.org/10.1016/j.ecoleng.2010.11.027.

Bouma, T.J., van Belzen, J., Balke, T., van Dalen, J., Klaassen, P., Hartog, A.M., Callaghan, D.P., Hu, Z., Stive, M.J.F., Temmerman, S., Herman, P.M.J., 2016. Short-term mudflat dynamics drive long-term cyclic salt marsh dynamics: Lateral Salt Marsh dynamics. Limnol. Oceanogr. 61, 2261–2275. https://doi.org/10.1002/lno.10374.

Brooks, H., Moeller, I., Spencer, T., Royse, K., Price, S., Kirkham, M., 2022. How strong are salt marshes? Geotechnical properties of coastal wetland soils. Earth Surf. Process. Landf. 47, 1390–1408. https://doi.org/10.1002/esp.5322.

Cadigan, J.A., Jafari, N.H., Wang, N., Chen, Q., Zhu, L., Harris, B.D., Ding, Y., 2023. Near-continuous monitoring of a coastal salt marsh margin: implications for predicting marsh edge erosion. Earth Surf. Process. Landf. 48, 1362–1373. https://doi.org/10.1002/esp.5554.

Cahoon, D.R., 2006. A review of major storm impacts on coastal wetland elevations. Estuaries Coasts: J ERF 29, 889–898. https://doi.org/10.1007/BF02798648.

Cao, H., Zhu, Z., Herman, P.M.J., Temmerman, S., Smit, J., Zhang, L., Yuan, L., Bouma, T.J., 2021. Plant traits determining biogeomorphic landscape dynamics: a study on clonal expansion strategies driving cliff formation at marsh edges. Limnol. Oceanogr. 66, 3754–3767. https://doi.org/10.1002/lno.11915.

Chang, K.-A., Hsu, T.-J., Liu, P.L.-F., 2005. Vortex generation and evolution in water waves propagating over a submerged rectangular obstacle: part II. Cnoidal waves. Coast. Eng. 52, 257–283. https://doi.org/10.1016/j.coastaleng.2004.11.006.

Chen, H., Adrian, R.J., Zhong, Q., Wang, X., 2014. Analytic solutions for three dimensional swirling strength in compressible and incompressible flows. Phys. Fluids 26, 081701. https://doi.org/10.1063/1.4893343.

Chirol, C., Spencer, K.L., Carr, S.J., Möller, I., Evans, B., Lynch, J., Brooks, H., Royse, K. R., 2021. Effect of vegetation cover and sediment type on 3D subsurface structure and shear strength in saltmarshes. Earth Surf. Process. Landf. 46, 2279–2297. https://doi.org/10.1002/esp.5174.

Chmura, G.L., Anisfeld, S.C., Cahoon, D.R., Lynch, J.C., 2003. Global carbon sequestration in tidal, saline wetland soils. Glob. Biogeochem. Cycles 17. https://doi.org/10.1029/2002GB001917.

Colosimo, I., de Vet, P.L.M., van Maren, D.S., Reniers, A.J.H.M., Winterwerp, J.C., van Prooijen, B.C., 2020. The impact of wind on flow and sediment transport over intertidal flats. JMSE 8, 910. https://doi.org/10.3390/jmse8110910.

Costanza, R., Farber, S.C., Maxwell, J., 1989. Valuation and management of wetland ecosystems. Ecol. Econ. 1, 335–361.

Dean, R.G., Dalrymple, R.W., 1991. Water wave mechanics for engineers and scientists. In: Advanced Series on Ocean Engineering. World Scientific, Singapore.

Doody, J.P., 1992. Sea defence and nature conservation: threat or opportunity. Aquat. Conserv. 2, 275–283. https://doi.org/10.1002/aqc.3270020307.

Duarte, C.M., Losada, I.J., Hendriks, I.E., Mazarrasa, I., Marbà, N., 2013. The role of coastal plant communities for climate change mitigation and adaptation. Nat. Clim. Change 3, 961–968. https://doi.org/10.1038/nclimate1970.

Dzimballa, S., Willemsen, P.W.J.M., Kitsikoudis, V., Borsje, B.W., Augustijn, D.C.M., 2024. Numerical modelling of biogeomorphological processes in salt marsh development: do short-term vegetation dynamics influence long-term development? Geomorphology 471, 109534. https://doi.org/10.1016/j.geomorph.2024.109534.

Edmonds, D.A., Caldwell, R.L., Brondizio, E.S., Siani, S.M.O., 2020. Coastal flooding will disproportionately impact people on river deltas. Nat. Commun. 11, 4741. https://doi.org/10.1038/s41467-020-18531-4.

Evans, B.R., Brooks, H., Chirol, C., Kirkham, M.K., Möller, I., Royse, K., Spencer, K., Spencer, T., 2022. Vegetation interactions with geotechnical properties and erodibility of salt marsh sediments. Estuar. Coast Shelf Sci. 265, 107713. https://doi.org/10.1016/j.ecss.2021.107713.

Evans, B.R., Möller, I., Spencer, T., 2021. Topological and morphological controls on morphodynamics of Salt Marsh interiors. J. Mar. Sci. Eng. 9, 311. https://doi.org/10.3390/jmse9030311.

Fagherazzi, S., 2014. Storm-proofing with marshes. Nat. Geosci. 7, 701–702. https://doi.org/10.1038/ngeo2262.

Fagherazzi, S., FitzGerald, D.M., Fulweiler, R.W., Hughes, Z., Wiberg, P.L., McGlathery, K.J., Morris, J.T., Tolhurst, T.J., Deegan, L.A., Johnson, D.S., 2013. 12.12 ecogeomorphology of salt marshes. In: Treatise on Geomorphology. Elsevier, pp. 182–200. https://doi.org/10.1016/B978-0-12-374739-6.00329-8.

Feagin, R.A., Lozada-Bernard, S.M., Ravens, T.M., Möller, I., Yeager, K.M., Baird, A.H., 2009. Does vegetation prevent wave erosion of salt marsh edges? Proc. Natl. Acad. Sci. U. S. A. 106, 10109–10113. https://doi.org/10.1073/pnas.0901297106.

Finotello, A., Marani, M., Carniello, L., Pivato, M., Roner, M., Tommasini, L., D'alpaos, A., 2020. Control of wind-wave power on morphological shape of salt marsh margins. Water Sci. Eng. 13, 45–56. https://doi.org/10.1016/j.wse.2020.03.006.

Francalanci, S., Bendoni, M., Rinaldi, M., Solari, L., 2013. Ecomorphodynamic evolution of salt marshes: experimental observations of bank retreat processes. Geomorphology 195, 53–65. https://doi.org/10.1016/j.geomorph.2013.04.026.

French, J., 2019. Tidal salt marshes. In: Coastal Wetlands. Elsevier, pp. 479–517. https://doi.org/10.1016/B978-0-444-63893-9.00014-9.

Gedan, K.B., Kirwan, M.L., Wolanski, E., Barbier, E.B., Silliman, B.R., 2011. The present and future role of coastal wetland vegetation in protecting shorelines: answering recent challenges to the paradigm. Clim. Change 106, 7–29. https://doi.org/10.1007/s10584-010-0003-7.

Houttuijn Bloemendaal, L.J., FitzGerald, D.M., Hughes, Z.J., Novak, A.B., Georgiou, I.Y., 2023. Reevaluating the wave power-salt marsh retreat relationship. Sci. Rep. 13, 2884. https://doi.org/10.1038/s41598-023-30042-y.

Huang, C.-J., Dong, C.-M., 2001. On the interaction of a solitary wave and a submerged dike. Coast. Eng. 43, 265–286. https://doi.org/10.1016/S0378-3839(01)00017-5.

Jadhav, R., 2012. Field Investigation of Wave and Surge Attenuation in Salt Marsh Vegetation and Wave Climate in a Shallow Estuary (Doctor of Philosophy). Louisiana State University and Agricultural and Mechanical College. https://doi.org/10.31390/gradschool_dissertations.3939.

Jeong, J., Hussain, F., 1995. On the identification of a vortex. J. Fluid Mech. 285, 69–94. https://doi.org/10.1017/S0022112095000462.

Karimpour, A., Chen, Q., Twilley, R.R., 2016. A field study of how wind waves and currents May contribute to the deterioration of saltmarsh fringe. Estuaries Coasts 39, 935–950. https://doi.org/10.1007/s12237-015-0047-z.

Kirwan, M.L., Temmerman, S., Skeehan, E.E., Guntenspergen, G.R., Fagherazzi, S., 2016. Overestimation of marsh vulnerability to sea level rise. Nat. Clim. Change 6, 253–260. https://doi.org/10.1038/nclimate2909.

Lavidas, G., Polinder, H., 2019. North Sea Wave Database (NSWD) and the need for reliable resource data: a 38 year database for metocean and wave energy assessments. Atmosphere 10, 551. https://doi.org/10.3390/atmos10090551.

Lee, J.-Y., Marotzke, J., 2021. Chapter 4: future global climate: Scenario-based projections and near-term information. In: Climate Change 2021: the Physical Science Basis. Contribution of Working Group I to the Sixth Assessment Report of the Intergovernmental Panel on Climate Change. Cambridge University Press, Cambridge, United Kingdom and New York, NY, USA.

Leonardi, N., Ganju, N.K., Fagherazzi, S., 2016. A linear relationship between wave power and erosion determines salt-marsh resilience to violent storms and hurricanes. Proc. Natl. Acad. Sci. U. S. A. 113, 64–68. https://doi.org/10.1073/pnas.1510095112.

Lin, C., Chang, S.-C., Ho, T.-C., Chang, K.-A., 2006. Laboratory observation of solitary wave propagating over a submerged rectangular dike. J. Eng. Mech. 132, 545–554. https://doi.org/10.1061/(ASCE)0733-9399(2006)132:5(545.

Lin, M.Y., Huang, L.H., 2010. Vortex shedding from a submerged rectangular obstacle attacked by a solitary wave. J. Fluid Mech. 651, 503–518. https://doi.org/10.1017/S0022112010000145.

Lohrmann, A., Cabrera, R., Kraus, N.C., 1994. Acoustic-Doppler velocimeter (ADV) for laboratory use. Fundamentals and Advancements in Hydraulic Measurements and Experimentation Proceedings, pp. 351–365.

Luhar, M., Nepf, H.M., 2016. Wave-induced dynamics of flexible blades. J. Fluid Struct. 61, 20–41. https://doi.org/10.1016/j.jfluidstructs.2015.11.007.

Marani, M., D'Alpaos, A., Lanzoni, S., Santalucia, M., 2011. Understanding and predicting wave erosion of marsh edges. Geophys. Res. Lett. 38. https://doi.org/10.1029/2011GL048995.

Marin-Diaz, B., van der Wal, D., Kaptein, L., Martinez-Garcia, P., Lashley, C.H., de Jong, K., Nieuwenhuis, J.W., Govers, L.L., Olff, H., Bouma, T.J., 2023. Using salt marshes for coastal protection: effective but hard to get where needed most. J. Appl. Ecol. 1–16. https://doi.org/10.1111/1365-2664.14413, 00.

Mariotti, G., Fagherazzi, S., 2013. Critical width of tidal flats triggers marsh collapse in the absence of sea-level rise. Proc. Natl. Acad. Sci. 110, 5353–5356. https://doi.org/10.1073/pnas.1219600110.

Mariotti, G., Fagherazzi, S., 2010. A numerical model for the coupled long-term evolution of salt marshes and tidal flats. J. Geophys. Res.: Earth Surf. 115. https://doi.org/10.1029/2009JF001326.

Marshall, J.R., 1962. The morphology of the upper Solway salt marshes. Scott. Geogr. Mag. 78, 81–99. https://doi.org/10.1080/00369226208735859.

Maza, M., Lara, J.L., Losada, I.J., Ondiviela, B., Trinogga, J., Bouma, T.J., 2015. Large-scale 3-D experiments of wave and current interaction with real vegetation. Part 2: experimental analysis. Coast. Eng. 106, 73–86. https://doi.org/10.1016/j.coastaleng.2015.09.010.

Mcowen, C.J., Weatherdon, L.V., Bochove, J.-W.V., Sullivan, E., Blyth, S., Zockler, C., Stanwell-Smith, D., Kingston, N., Martin, C.S., Spalding, M., Fletcher, S., 2017. A global map of saltmarshes. Biodivers. Data J., e11764 https://doi.org/10.3897/BDJ.5.e11764.

Méndez, F.J., Losada, I.J., Losada, M.A., 1999. Hydrodynamics induced by wind waves in a vegetation field. J. Geophys. Res.: Oceans 104, 18383–18396. https://doi.org/10.1029/1999JC900119.

Millennium Ecosystem Assessment, 2005. In: Ecosystems and Human Well-Being: Wetlands and Water Synthesis. World Resources Institute, Washington, DC.

Möller, I., Kudella, M., Rupprecht, F., Spencer, T., Paul, M., van Wesenbeeck, B.K., Wolters, G., Jensen, K., Bouma, T.J., Miranda-Lange, M., Schimmels, S., 2014. Wave attenuation over coastal salt marshes under storm surge conditions. Nat. Geosci. 7, 727–731. https://doi.org/10.1038/ngeo2251.

Möller, I., Spencer, T., 2002. Wave dissipation over macro-tidal saltmarshes: effects of marsh edge typology and vegetation change. J. Coast Res. 36, 506–521. https://doi.org/10.2112/1551-5036-36.sp1.506.

Nepf, H.M., 1999. Drag, turbulence, and diffusion in flow through emergent vegetation. Water Resour. Res. 35, 479–489. https://doi.org/10.1029/1998WR900069.

Neumann, B., Vafeidis, A.T., Zimmermann, J., Nicholls, R.J., 2015. Future Coastal population growth and exposure to sea-level rise and Coastal flooding - a global assessment. PLoS One 10, e0118571. https://doi.org/10.1371/journal.pone.0118571.

Nicholls, R.J., Brown, S., Hanson, S., Hinkel, J., 2010. Economics of Coastal Zone : Adaptation to Climate Change (No. 10), Development and Climate Change Discussion Paper. World Bank Group, Washington, D.C.

Nortek, A.S., 2018. Comprehensive Manual for Velocimeters. No. N3015- 030).

Priestas, A.M., Mariotti, G., Leonardi, N., Fagherazzi, S., 2015. Coupled wave energy and erosion dynamics along a salt marsh boundary, Hog Island Bay, Virginia, USA. J. Mar. Sci. Eng. 3, 1041–1065. https://doi.org/10.3390/jmse3031041.

Reed, D., van Wesenbeeck, B., Herman, P.M.J., Meselhe, E., 2018. Tidal flat-wetland systems as flood defenses: understanding biogeomorphic controls. Estuar. Coast Shelf Sci. 213, 269–282. https://doi.org/10.1016/j.ecss.2018.08.017.

Rey, V., Belzons, M., Guazzelli, E., 1992. Propagation of surface gravity waves over a rectangular submerged bar. J. Fluid Mech. 235, 453–479. https://doi.org/10.1017/S0022112092001186.

Schoutens, K., Stoorvogel, M., van den Berg, M., van den Hoven, K., Bouma, T.J., Aarninkhof, S., Herman, P.M.J., van Loon-Steensma, J.M., Meire, P., Schoelynck, J., Peeters, P., Temmerman, S., 2022. Stability of a tidal marsh under very high flow velocities and implications for nature-based flood defense. Front. Mar. Sci. 9.

Spencer, T., Möller, I., Rupprecht, F., Bouma, T.J., Van Wesenbeeck, B.K., Kudella, M., Paul, M., Jensen, K., Wolters, G., Miranda-Lange, M., Schimmels, S., 2016. Salt marsh surface survives true-to-scale simulated storm surges. Earth Surf. Process. Landf. 41, 543–552. https://doi.org/10.1002/esp.3867.

Stark, J., Van Oyen, T., Meire, P., Temmerman, S., 2015. Observations of tidal and storm surge attenuation in a large tidal marsh. Limnol. Oceanogr. 60, 1371–1381. https://doi.org/10.1002/lno.10104.

Stoorvogel, M.M., van Belzen, J., Temmerman, S., Wiesebron, L.E., Fivash, G.S., van Ijzerloo, L., van de Koppel, J., Bouma, T.J., 2024. Salt marshes for nature-based flood defense: sediment type, drainage, and vegetation drive the development of strong sediment beds. Ecol. Eng. 207, 107335. https://doi.org/10.1016/j.ecoleng.2024.107335.

Sutton-Grier, A.E., Wowk, K., Bamford, H., 2015. Future of our coasts: the potential for natural and hybrid infrastructure to enhance the resilience of our coastal communities, economies and ecosystems. Environ. Sci. Pol. 51, 137–148. https://doi.org/10.1016/j.envsci.2015.04.006.

Suzuki, T., Klaassen, P.C., 2011. Hydrodynamics on seedlings of halophytic plants around a salt marsh cliff. J. Coast Res. 6.

Temmerman, S., Horstman, E.M., Krauss, K.W., Mullarney, J.C., Pelckmans, I., Schoutens, K., 2023. Marshes and mangroves as nature-based coastal storm buffers. Annu. Rev. Mar. Sci. 15, 95–118. https://doi.org/10.1146/annurev-marine-040422-092951.

Temmerman, S., Meire, P., Bouma, T.J., Herman, P.M.J., Ysebaert, T., De Vriend, H.J., 2013. Ecosystem-based coastal defence in the face of global change. Nature 504, 79–83. https://doi.org/10.1038/nature12859.

Thielicke, W., Sonntag, R., 2021. Particle Image Velocimetry for MATLAB: Accuracy and enhanced algorithms in PIVlab. JORS 9, 12. https://doi.org/10.5334/jors.334.

Ting, F.C.K., Kim, Y.-K., 1994. Vortex generation in water waves propagating over a submerged obstacle. Coast. Eng. 24, 23–49. https://doi.org/10.1016/0378-3839(94)90025-6.

Tonelli, M., Fagherazzi, S., Petti, M., 2010. Modeling wave impact on salt marsh boundaries. J. Geophys. Res.: Oceans 115. https://doi.org/10.1029/2009JC006026.

Trosclair, K.J., 2013. Wave transformation at a saltmarsh edge and resulting marsh edge erosion. Observations and Modeling. University of New Orleans Theses and Dissertations), New Orleans.

Valentine, K., Mariotti, G., 2019. Wind-driven water level fluctuations drive marsh edge erosion variability in microtidal coastal bays. Cont. Shelf Res. 176, 76–89. https://doi.org/10.1016/j.csr.2019.03.002.

van de Koppel, J., Van der Wal, D., Bakker, J.P., Herman, P.M.J., 2005. Self-organization and vegetation collapse in Salt Marsh ecosystems. Am. Nat. 165, E1–E12. https://doi.org/10.1086/426602.

van der Wal, D., van Dalen, J., Willemsen, P.W.J.M., Borsje, B.W., Bouma, T.J., 2023. Gradual versus episodic lateral saltmarsh cliff erosion: evidence from Terrestrial Laser Scans (TLS) and Surface Elevation Dynamics (SED) sensors. Geomorphology 426, 108590. https://doi.org/10.1016/j.geomorph.2023.108590.

Van der Wal, D., Wielemaker-Van den Dool, A., Herman, P.M.J., 2008. Spatial patterns, rates and mechanisms of saltmarsh cycles (Westerschelde, the Netherlands). Estuar. Coast Shelf Sci. 76, 357–368. https://doi.org/10.1016/j.ecss.2007.07.017.

van Eerdt, M.M., 1985. The influence of vegetation on erosion and accretion in salt marshes of the Oosterschelde, the Netherlands. Vegetatio 62, 367–373. https://doi.org/10.1007/BF00044763.

van Wesenbeeck, B.K., Mulder, J.P.M., Marchand, M., Reed, D.J., de Vries, M.B., de Vriend, H.J., Herman, P.M.J., 2014. Damming deltas: a practice of the past? Towards nature-based flood defenses. Estuar. Coast Shelf Sci. 140, 1–6. https://doi.org/10.1016/j.ecss.2013.12.031.

Visser, J.M., Midway, S., Baltz, D.M., Sasser, C.E., 2019. Chapter 15 - ecosystem structure of tidal saline marshes. In: Perillo, G.M.E., Wolanski, E., Cahoon, D.R., Hopkinson, C. S. (Eds.), Coastal Wetlands, second ed. Elsevier, pp. 519–538. https://doi.org/10.1016/B978-0-444-63893-9.00015-0.

Vuik, V., 2019. Building Safety with Nature: Salt Marshes for Flood Risk Reduction. Delft University of Technology. https://doi.org/10.4233/UUID:9339474C-3C48-437F-8AA5-4B908368C17E.

Vuik, V., Jonkman, S.N., Borsje, B.W., Suzuki, T., 2016. Nature-based flood protection: the efficiency of vegetated foreshores for reducing wave loads on coastal dikes. Coast. Eng. 116, 42–56. https://doi.org/10.1016/j.coastaleng.2016.06.001.

Vuik, V., Suh Heo, H.Y., Zhu, Z., Borsje, B.W., Jonkman, S.N., 2018. Stem breakage of salt marsh vegetation under wave forcing: a field and model study. Estuar. Coast Shelf Sci. 200, 41–58. https://doi.org/10.1016/j.ecss.2017.09.028.

Wang, H., van der Wal, D., Li, X., van Belzen, J., Herman, P.M.J., Hu, Z., Ge, Z., Zhang, L., Bouma, T.J., 2017. Zooming in and out: scale dependence of extrinsic and intrinsic factors affecting salt marsh erosion. J. Geophys. Res.: Earth Surf. 122, 1455–1470. https://doi.org/10.1002/2016JF004193.

Westerweel, J., 1997. Fundamentals of digital particle image velocimetry. Meas. Sci. Technol. 8, 1379–1392. https://doi.org/10.1088/0957-0233/8/12/002.

Willemsen, P.W.J.M., Borsje, B.W., Hulscher, S.J.M.H., Van der Wal, D., Zhu, Z., Oteman, B., Evans, B., Möller, I., Bouma, T.J., 2018. Quantifying bed level change at the transition of tidal flat and salt Marsh: can we understand the lateral location of the Marsh edge? J. Geophys. Res.: Earth Surf. 123, 2509–2524. https://doi.org/10.1029/2018JF004742.

Willemsen, P.W.J.M., Horstman, E.M., Bouma, T.J., Baptist, M.J., van Puijenbroek, M.E. B., Borsje, B.W., 2022. Facilitating salt marsh restoration: the importance of event-based bed level dynamics and seasonal trends in bed level change. Front. Mar. Sci. 8, 793235. https://doi.org/10.3389/fmars.2021.793235.

WinklerPrins, L., Lacy, J.R., Stacey, M.T., Logan, J.B., Stevens, A.W., 2024. Seasonality of retreat rate of a wave-exposed marsh edge. J. Geophys. Res.: Earth Surf. 129, e2023JF007468. https://doi.org/10.1029/2023JF007468.

Zhang, X., Lin, P., Nepf, H., 2022. A wave damping model for flexible marsh plants with leaves considering linear to weakly nonlinear wave conditions. Coast. Eng. 175, 104124. https://doi.org/10.1016/j.coastaleng.2022.104124.

Zhang, X., Nepf, H., 2021. Wave-induced reconfiguration of and drag on marsh plants. J. Fluids Struct. 100, 103192. https://doi.org/10.1016/j.jfluidstructs.2020.103192.

Zhao, K., Liu, P.L-F., 2022. On Stokes wave solutions. Proc. R. Soc. A. 478, 20210732. https://doi.org/10.1098/rspa.2021.0732.
Zhou, J., Adrian, R.J., Balachandar, S., Kendall, T.M., 1999. Mechanisms for generating coherent packets of hairpin vortices in channel flow. J. Fluid Mech. 387, 353–396. https://doi.org/10.1017/S002211209900467X.
Zhu, Z., Vuik, V., Visser, P.J., Soens, T., van Wesenbeeck, B., van de Koppel, J., Jonkman, S.N., Temmerman, S., Bouma, T.J., 2020. Historic storms and the hidden value of coastal wetlands for nature-based flood defence. Nat. Sustain. 3, 853–862. https://doi.org/10.1038/s41893-020-0556-z.